AGU PUBLICATIONS

Journal of Advances in Modeling Earth Systems



RESEARCH ARTICLE

10.1002/2014MS000366

Key Points:
- Moist convection has little impact on initial asymmetric wave growth
- Main source term of asymmetric KE involves radial shear of primary circulation
- Moist convection reduces intensity loss otherwise caused by instabilities

Correspondence to:
J. Naylor,
jasonnaylor@purdue.edu

Citation:
Naylor, J., and D. A. Schecter (2014), Evaluation of the impact of moist convection on the development of asymmetric inner core instabilities in simulated tropical cyclones, *J. Adv. Model. Earth Syst.*, *6*, 1027–1048, doi:10.1002/2014MS000366.

Received 22 JUL 2014
Accepted 4 OCT 2014
Accepted article online 13 OCT 2014
Published online 14 NOV 2014

This is an open access article under the terms of the Creative Commons Attribution-NonCommercial-NoDerivs License, which permits use and distribution in any medium, provided the original work is properly cited, the use is non-commercial and no modifications or adaptations are made.

Evaluation of the impact of moist convection on the development of asymmetric inner core instabilities in simulated tropical cyclones

Jason Naylor[1,2] and David A. Schecter[1]

[1]NorthWest Research Associates, Boulder, Colorado, USA, [2]Now at Department of Earth, Atmospheric, and Planetary Sciences, Purdue University, West Lafayette, Indiana

Abstract This paper examines the nature and consequences of inner core instabilities in several intense tropical cyclones (TCs) simulated with a cloud-resolving numerical model. The initial wave growth leading to polygonal eyewalls and mesovortices in each TC is shown to closely resemble that found in a dry non-convective vortex with the same primary circulation. Such agreement is reasonable partly because the bulk of the cloudy eyewall updraft is outside the vorticity ring in which the instability occurs. An energetic analysis of the TC instability verifies that the symmetric secondary circulation contributes relatively little to the early growth of eddy kinetic energy. On a longer time scale, isentropic potential vorticity mixing triggered by the instability irreversibly reduces the maximum wind speed of the dry vortex. In the more realistically simulated TC, moist convection modulates the mixing and regenerates the broken vorticity ring. Eventually, the maximum wind speed of the TC and the local parameters that determine its theoretical magnitude return to within a few percent of their preinstability values. It is found that the time scale for wind speed restoration is sensitive to the surface drag coefficient. The long-term effects of inner core instability on precipitation are briefly addressed.

1. Introduction

Intense tropical cyclones (TCs) tend to develop potential vorticity (PV) distributions that are strongly peaked in the vicinity of the eyewall [e.g., *Hausman et al*., 2006; *Bell and Montgomery*, 2008; *Rogers et al*., 2013]. In theory, such a condition can destabilize the TC by enabling the growth of phase-locked counterpropagating vortex Rossby waves (VRWs) on opposite sides of the PV peak [cf. *Montgomery and Shapiro*, 1995; *Michalke and Timme*, 1967]. This so-called barotropic instability can generate mesovortices and initiate horizontal mixing between the eye and eyewall [e.g., *Schubert et al*., 1999; *Hendricks and Schubert*, 2010]. The consequences on TC intensity are potentially significant and continue to be researched.

The nature of barotropic instability has been studied extensively in nondivergent two-dimensional (2-D) models, where absolute vertical vorticity and PV are essentially the same. In this context, it has been shown that the width of the off-center vorticity peak and its magnitude relative to vorticity in the eye largely determine the azimuthal wave number and growth rate of the most unstable mode [*Schubert et al*., 1999; *Kossin and Eastin*, 2001; *Hendricks et al*., 2009]. In principle, the prevailing instability of a three-dimensional (3-D) TC-like vortex could have a baroclinic nature [*Kwon and Frank*, 2005]. However, the dominant 3-D instabilities of dry vortices resembling intense TCs are usually similar to their 2-D barotropic counterparts [*Nolan and Montgomery*, 2002; *Hendricks and Schubert*, 2010].

A number of observational studies have appealed to barotropic instability to explain the features and behavior of real-world TCs. *Muramatsu* [1986] suggested that the polygonal eye structure of typhoon 8019 could have been due to barotropic instability on the inner edge of the eyewall. *Reasor et al*. [2000] used dual-Doppler radar data to examine the low-level asymmetric vorticity structure of Hurricane Olivia (1994). The prevailing wavenumber-2 feature proved consistent with the most unstable mode of barotropic instability in an analogous 2-D vortex. Horizontal mixing brought on by the instability was offered as a possible mechanism for broadening Olivia's symmetric vorticity distribution during the observation period. *Kossin and Eastin* [2001] used aircraft flight-level data to show that strong TCs commonly transition between two distinct regimes. The first regime has a well-defined peak of angular velocity in the eyewall, and the second

© 2014. The Authors.

has an angular velocity profile that decays monotonically with increasing radius. The observed transition from the first to second regime was found to agree reasonably well with the effect of vorticity mixing following barotropic instability in fully nonlinear 2-D simulations. *Kossin and Schubert* [2004] and *Montgomery et al*. [2006] noted that the striking mesovortices of Hurricane Isabel (2006) likely resulted from barotropic or combined barotropic-baroclinic instability. *Hendricks et al*. [2012] maintained that barotropic instability was the most likely cause of high wave number eyewall asymmetries during a rapid intensification phase of Hurricane Dolly (2008).

From a theoretical perspective, it is not entirely clear how moist convection should affect the inner core instabilities of a TC. The presence of mean secondary circulation could alter the growth rate and structure of the most unstable mode, as has been shown for tornado-like vortices [cf. *Rotunno*, 1978; *Nolan and Farrell*, 1999; *Nolan*, 2012]. So too could the reduction of static stability by cloud coverage [*Schecter and Montgomery*, 2007]. *Nolan and Montgomery* [2002] further noted that "convectively coupled VRWs" in realistically simulated TCs may have fundamental differences with the VRWs found in the growing modes of dry TC-like vortices.

A simple approach toward understanding the effect of eyewall convection on inner core instability is to apply some form of eyewall forcing in a 2-D model. *Rozoff et al*. [2009] parameterized eyewall convection in a dissipative, nondivergent 2-D model by adding a persistent (but limited) vorticity source to an annular region of the TC. The initial development of barotropic instability in the forced vorticity ring proved similar to that which occurs in an unforced ring. However, continual regeneration of the vorticity ring prevented the vortex from relaxing to a centrally peaked monopole. The long-term evolution was instead characterized by repeated episodes of restrained mixing events. *Hendricks et al*. [2014] extended the simulations of *Rozoff et al*. [2009] to a shallow water model with an annular mass sink. The mass sink mimicked diabatic eyewall convection and created a ring of elevated PV. The barotropic instability of this ring was similar to that found in unforced 2-D simulations. However, both *Rozoff et al*. [2009] and *Hendricks et al*. [2014] acknowledged shortcomings of their prescribed forcing techniques and advocated additional experiments with 3-D full-physics models.

Of course, there have been many previous studies investigating the nature of inner core asymmetries that spontaneously develop in realistically simulated TCs [*Chen and Yau*, 2001; *Wang*, 2002; *Yang et al*., 2007; *Wang*, 2007; *Kwon and Frank*, 2008; *Persing et al*., 2013]. Barotropic or combined barotropic-baroclinic instability of the simulated TC is often cited as a potential mechanism for the development of these asymmetries. As discussed by *Persing et al*. [2013], such an interpretation may often oversimplify mechanisms that involve more complex convective processes. The full-physics simulations presented here are specially designed to eliminate generic noise (stochastic convection) from the initial state of a mature TC and thereby isolate the dominant instability for analysis.

While it is important to understand the time scale and spatial structure of the dominant inner core instability, it may be more important to understand its consequences on TC intensity. In dry simulations, barotropic instability can initiate vigorous horizontal mixing that spins up the eye and intensifies the central pressure deficit while simultaneously decreasing the maximum tangential velocity [*Schubert et al*., 1999; *Hendricks and Schubert*, 2010]. By transporting angular momentum away from the region of maximum wind speed, recurrent barotropic instability could partly explain why TCs in 3-D full-physics simulations tend to have weaker sustained winds than their axisymmetric counterparts [*Yang et al*., 2007; *Bryan*, 2012]. The effect of barotropic instability on the thermodynamic maintenance of TC intensity must also be considered. *Yang et al*. [2007] proposed that asymmetric fluctuations (partly due to instability) can limit TC intensity by reducing eyewall tilt and weakening downdrafts in the vicinity of the radius of maximum wind. They argued that a state of weaker downdrafts diminishes the air-sea disequilibrium required to extract latent and sensible heat from the sea surface. In contrast, *Bell and Montgomery* [2008] proposed that eyewall mesovortices created by instability helped Hurricane Isabel (2006) maintain its strength when passing over cooler water by transporting high entropy air from the eye into the eyewall.

One goal of the present study is to assess the influence of moist convection on the growth rate and structure of the dominant asymmetry that emerges from the inner core instability of an intense TC. A second goal is to clarify how moist convection modifies the effect of instability on vortex intensity. These goals are largely achieved by quantitatively comparing instabilities in full-physics simulations to those in dry

© 2014. The Authors.

simulations where the vortices have the same tangential wind structure. The remainder of this paper is organized as follows. Section 2 discusses the methodology and model configurations. Results from the dry and moist simulations are presented in section 3. Discussion of the results are given in section 4, and the conclusions are given in section 5.

2. Methodology

Two types of 3-D simulations were performed: one configuration included moisture, surface fluxes, and radiation (herein referred to as moist simulations) while the second configuration excluded these elements (herein referred to as dry simulations). All 3-D simulations were conducted on a rectangular grid with version 17 of Cloud Model 1 (CM1; *Bryan and Fritsch* [2002]). The horizontal grid spacing was 250 m over the central 175 km of each horizontal coordinate. Outside the central region, the grid spacing gradually increased to 10 km. The horizontal grid consisted of 1080 $\times$ 1080 grid points covering a domain of 2122.5 $\times$ 2122.5 km^2. In the vertical direction, grid spacing was constant (Δz=100 m) below z=3 km. Above this level, grid spacing gradually increased to 500 m. There were 68 grid points in the vertical, and the model top was 30 km. Lateral boundaries were open, and Rayleigh damping was applied above z=26 km. Subgrid turbulence was parameterized using a first-order closure scheme in which the eddy viscosity is proportional to the flow deformation (iturb=3 option in the CM1 name list). An f-plane approximation was used with the Coriolis parameter f set to 5×10^{-5} s^{-1}. The horizontally homogeneous base state of the atmosphere was initialized with the sounding from *Rotunno and Emanuel* [1987] (hereafter RE87).

In the moist simulations, cloud processes were represented by a simple three-class (water vapor, cloud water, rain) microphysics parameterization. Newtonian relaxation capped at 2 K d^{-1} was applied to the potential temperature field to approximate radiative cooling (cf. RE87). The horizontal mixing length in the turbulence parameterization was defined to be 100 m, whereas the vertical mixing length was height dependent and approached a value of 200 m at elevations greater than 1 km. Surface fluxes of enthalpy and momentum were parameterized using bulk aerodynamic formulations. The exchange coefficients of enthalpy (c_e) and momentum (c_d) were specified as constant values in both space and time. For all simulations, c_e was set to 1.5×10^{-3}. This value of c_e is on the high end of recent observations [e.g., *Bell et al.*, 2012], but smaller than that predicted at major hurricane wind speeds by *Andreas* [2011]. The simulations presented herein use this value of c_e paired with one of the following values for c_d: 5×10^{-3} (c_e/c_d=0.3), 3×10^{-3} (c_e/c_d=0.5), or 1.5×10^{-3} (c_e/c_d=1).

All 3-D simulations were initialized with quasi steady state structures produced with an axisymmetric version of CM1. In the axisymmetric configuration, the fluid variables depend only on the cylindrical radius r, height z and time t. There is no variation in the azimuth λ. The axisymmetric simulations were configured as in the 3-D simulations. The radial domain extended to r = 1061.25 km and contained 540 grid points.

Moist axisymmetric simulations were initialized with a weak nonconvective vortex in gradient and hydrostatic balance. The tangential velocity (v) was specified by

$$v(r,z)=\frac{z_t-z}{z_t}\left\langle\left[v_c^2\left(\frac{r}{r_c}\right)^2\left(\left(\frac{2r_c}{r+r_c}\right)^3-\left(\frac{2r_c}{r_0+r_c}\right)^3\right)+\frac{f^2r^2}{4}\right]^{1/2}-\frac{fr}{2}\right\rangle, \quad (1)$$

in which v_c and r_c are the characteristic wind speed and radius of the vortex core, z_t is the maximum height of the vortex, and r_0 is outer radius of the vortex (cf. RE87). The velocity field is zero for $z \geq z_t$ and $r \geq r_0$. The parameter values were chosen to be v_c = 25 m s^{-1}, r_c =162.5 km, z_t = 20 km, and r_0 = 812.5 km.

After spin-up, all field variables in the moist axisymmetric simulations were time averaged and put onto a Cartesian grid to be used as basic initial conditions for the moist 3-D simulations. A pseudo-random perturbation was then added to the radial velocity to weakly excite a variety of asymmetric waves. The magnitude of this perturbation was scaled in proportion to the local strength of the primary circulation.

To initialize dry 3-D simulations, the quasi steady state tangential velocity, potential temperature, and Exner function from the moist axisymmetric simulations were first used as initial conditions for dry axisymmetric simulations. In these dry simulations, moisture, surface fluxes, and radiation were eliminated. The radial and vertical velocities were set to zero and the tangential velocity field was adjusted such that the maximum

© 2014. The Authors.

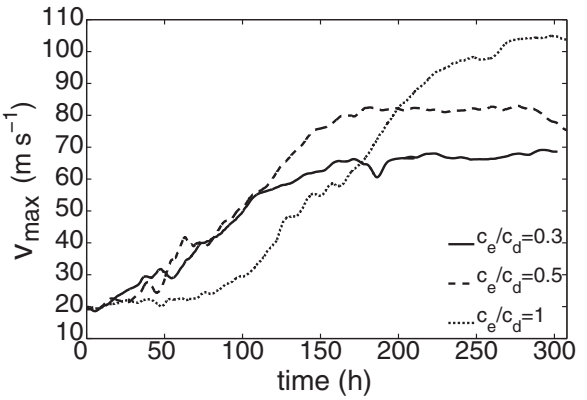

Figure 1. Time series of maximum tangential velocity for the moist axisymmetric simulations. A 6 h running mean was applied to smooth the data.

was at the lowest model level. The dry axisymmetric simulations were run for a total of 128 h. For the first 48 h, radial and vertical velocities were nudged toward zero and the tangential velocity was nudged back to the value at $t = 0$. The goal of this procedure was to preserve the quasi steady state tangential velocity structure from the moist axisymmetric simulations (particularly, the radial profile of vertical vorticity) while allowing the pressure and temperature fields to adjust to the removal of moisture and the secondary circulation. Experimentation revealed that in order to preserve the radial profile of vertical vorticity, subgrid turbulent dissipation needed to be reduced. Thus, in the dry simulations, the horizontal mixing length was 10 m and the height-dependent vertical mixing length approached a value of 10 m above $z = 1$ km. The quasi-steady state structures obtained from the dry axisymmetric simulations (typically from the last 10 h of run time) were converted to Cartesian coordinates and used for the initial conditions of the dry 3-D simulations. Pseudo-random radial velocity perturbations were added to the initial conditions with the same procedure used for the moist simulations. The mixing lengths in the subgrid turbulence parameterization of the dry 3-D simulations were the same as in the dry axisymmetric simulations. Although surface fluxes were absent in the dry simulations, each will be referred to by the ratio of c_e to c_d from the moist axisymmetric simulation that provided the tangential velocity field of the initial vortex.

3. Results

3.1. Preliminary Spin-Up Simulations

Time series of maximum tangential velocity from the moist axisymmetric spin-up simulations are shown in Figure 1. As expected, maximum tangential wind speed increases with the ratio of c_e to c_d [cf. *Emanuel* 1995]. All three simulations reach a quasi steady state at some point between $t = 200$ h and $t = 300$ h. "Steady state" was determined based on analysis of maximum tangential velocity (Figure 1) and vertical vorticity at select heights (not shown). A simulation was said to have reached a steady state when the variations in these fields over a 24 h period were smallest. Based on values of 10 m wind speed (not shown), the steady state intensities of the simulated TCs range from Category 2 ($c_e/c_d = 0.3$ simulation) to Category 5 ($c_e/c_d = 1$ simulation) on the Saffir-Simpson scale.

The steady structure of vertical vorticity (ζ) in the three simulations is shown in Figure 2. All three profiles possess a reversal in the radial gradient of ζ that reflects a similar reversal in the radial gradient of PV (not shown). As noted earlier, such reversal is conducive to shear flow instability. The $c_e/c_d = 0.3$ simulation has the smallest magnitude peak in the ζ annulus at $z = 0.78$ km (Figure 2a) while the $c_e/c_d = 1$ simulation has the largest amplitude peak (Figure 2c). The $c_e/c_d = 0.3$ simulation also exhibits a disruption in the off-center ζ peak around $z = 6$ km to $z = 8$ km which is not present in the other two simulations. An interesting feature that occurs in all three simulations is the branch of ζ that tilts radially outward with height and eventually separates from the main annulus just below $z = 4$ km. This feature is associated with the central region of the eyewall updraft.

3.2. Initial Development of Asymmetry in the 3-D Simulations

3.2.1. Wave Growth and Mesovortex Formation

Figure 3 shows horizontal cross sections of ζ at 30 min intervals in the three moist simulations. All three simulations produce discernible polygonal patterns in ζ by $t = 60$ min, and nascent mesovortices by $t = 90$ min. In the $c_e/c_d = 0.3$ simulation, six azimuthal segments are noticeable in ζ at $t = 90$ min (Figure 3c). In both the $c_e/c_d = 0.5$ and $c_e/c_d = 1$ simulations, five segments can be seen at $t = 90$ min (Figures 3f and 3i). Differences in the basic states of these simulations are presumably responsible for varying asymmetric structure.

© 2014. The Authors.

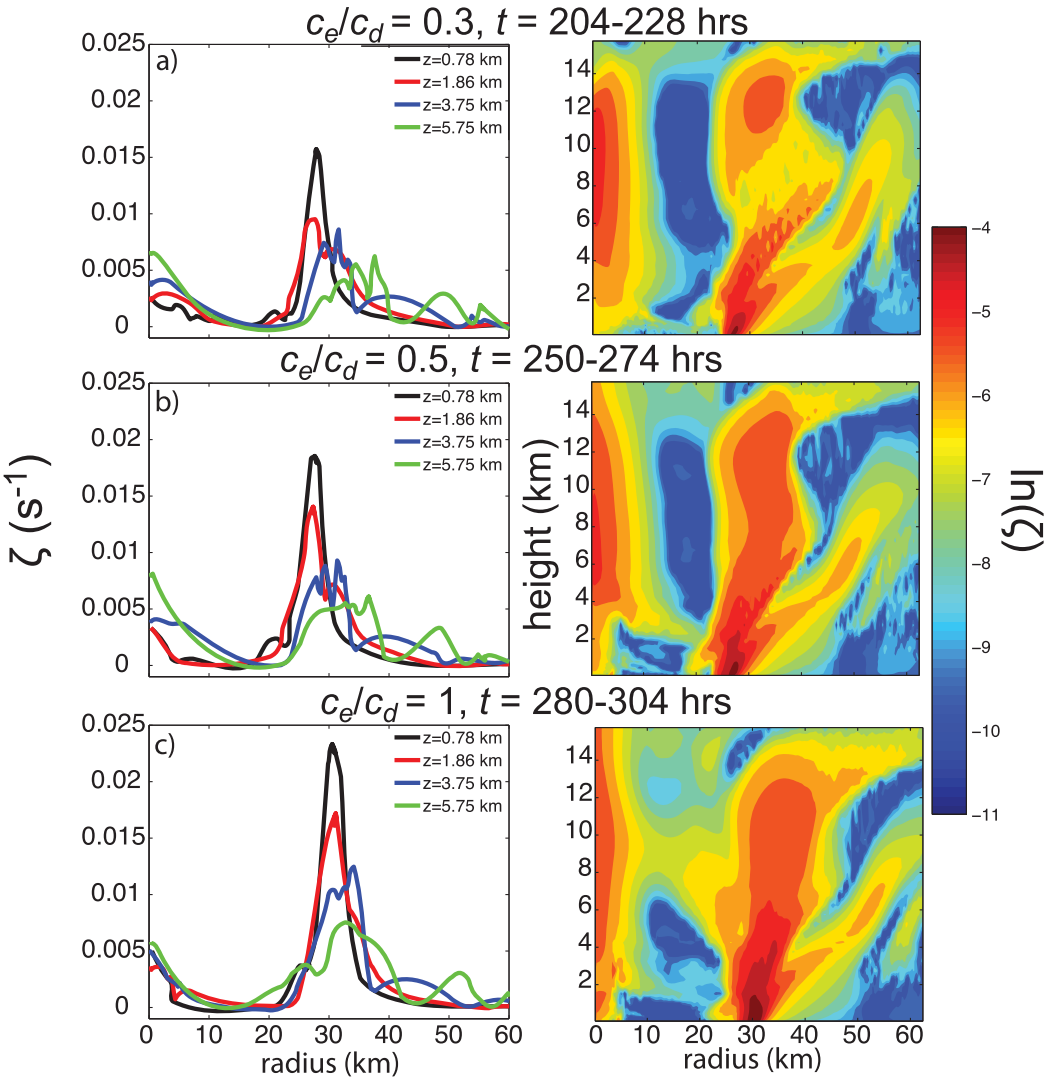

Figure 2. Time-averaged, quasi steady state profiles of vertical vorticity from the moist axisymmetric simulations with (a) c_e/c_d=0.3, (b) c_e/c_d=0.5, and (c) c_e/c_d=1. Left plots show radial profiles of ζ at select heights, while the plots on the right show the r,z structure of ln(ζ).

However, the main question at hand is whether or not asymmetric development in the moist simulations agrees with what occurs in the dry analog simulations.

To begin to address this question, the initial growth rates of asymmetries in the 3-D simulations were examined via a discrete Fourier transform of tangential velocity v:

$$\hat{v}_m(r,z,t) = \frac{1}{N}\sum_{j=0}^{N-1} v(r,j,z,t)e^{-i2\pi mj/N}, \tag{2}$$

where j is the azimuth in degrees, $N = 360$, and m is the azimuthal wave number. Figure 4 shows the growth of the squared amplitude of $\hat{v}_m$ during the first 90 min of simulation time. The plotted values of $|\hat{v}_m|^2$ are radially averaged over a 30 km interval centered on the initial radius of maximum wind (RMW) and vertically averaged from $z = 0.78$ km to $z = 2.75$ km.

Before nonlinear saturation is apparent, the fastest growing modes have wave numbers ranging from 4 to 6 and e-folding times (for $|\hat{v}_m|$) ranging from 15 to 20 min. Overall, the growth rates of the dominant modes are very similar between the moist simulations (Figure 4, left plots) and their dry counterparts (Figure 4, right plots). One minor difference is that wavenumber 3 tends to have greater significance in the dry simulations. Perhaps the most noticeable difference is seen between the moist simulation with c_e / c_d = 0.3 and

© 2014. The Authors.

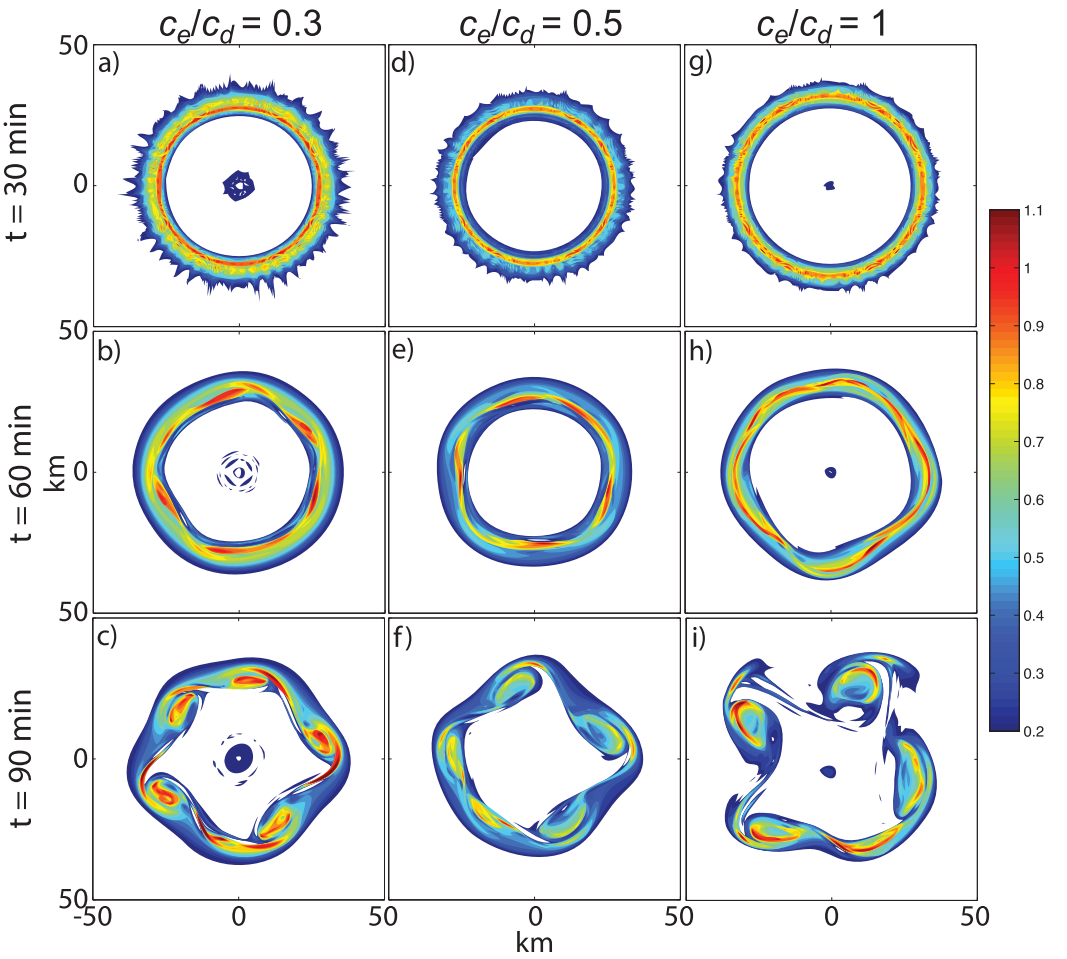

Figure 3. Horizontal cross sections of dimensionless vertical vorticity at z=1.2 km at select times from the moist simulations. In each simulation, vertical vorticity was normalized by the maximum value at t=0.

its dry counterpart. Here, the dry *e*-folding times for wavenumbers 4 and 5 are approximately 35% and 15% greater than their corresponding moist values. These discrepancies could be related to slightly different initial distributions of low-level ζ. Despite efforts to preserve the (r, z) structure of ζ when constructing the dry vortices, the large degree of supergradient flow in the $c_e/c_d = 0.3$ case complicated the balancing procedure near the surface. The final result was a dry, balanced vortex with a smaller peak amplitude in the ζ annulus below $z = 1$ km than its moist, unbalanced counterpart. Even though the $c_e/c_d = 0.5$ and $c_e/c_d = 1$ TCs also possess some amount of supergradient flow, the balancing process was more successful in these cases.

Next, the vertical structure of the asymmetries was examined. For this analysis, the Fourier coefficients of ζ were used to define the following normalized asymmetry parameter,

$$\chi(r,z,t)=\frac{\sum_{m=2}^{m=8}|\hat{\zeta}_m(r,z,t)|^2}{\max\limits_{r_1\le r\le r_2}\left[\hat{\zeta}_0^2(r,z,t)\right]}, \tag{3}$$

where r_1 = 15 km and r_2=50 km. The denominator in (3) is the squared maximum of the symmetric component of ζ at each vertical level. Figure 5 shows the r,z structure of χ at t=90 min for all three moist simulations. For c_e/c_d =0.3 and $c_e/c_d = 0.5$ (Figures 5a and 5b), the substantial part of the asymmetry extends to approximately 6 km in height, which is slightly higher than the extent of the mesovortices in the simulation of *Braun et al.* [2006]. The greatest asymmetry is seen when c_e/c_d=1 (Figure 5c). In this simulation, strong asymmetry extends up to z=10 km. Note that the stronger asymmetry in the c_e/c_d=1 simulation at t=90

© 2014. The Authors.

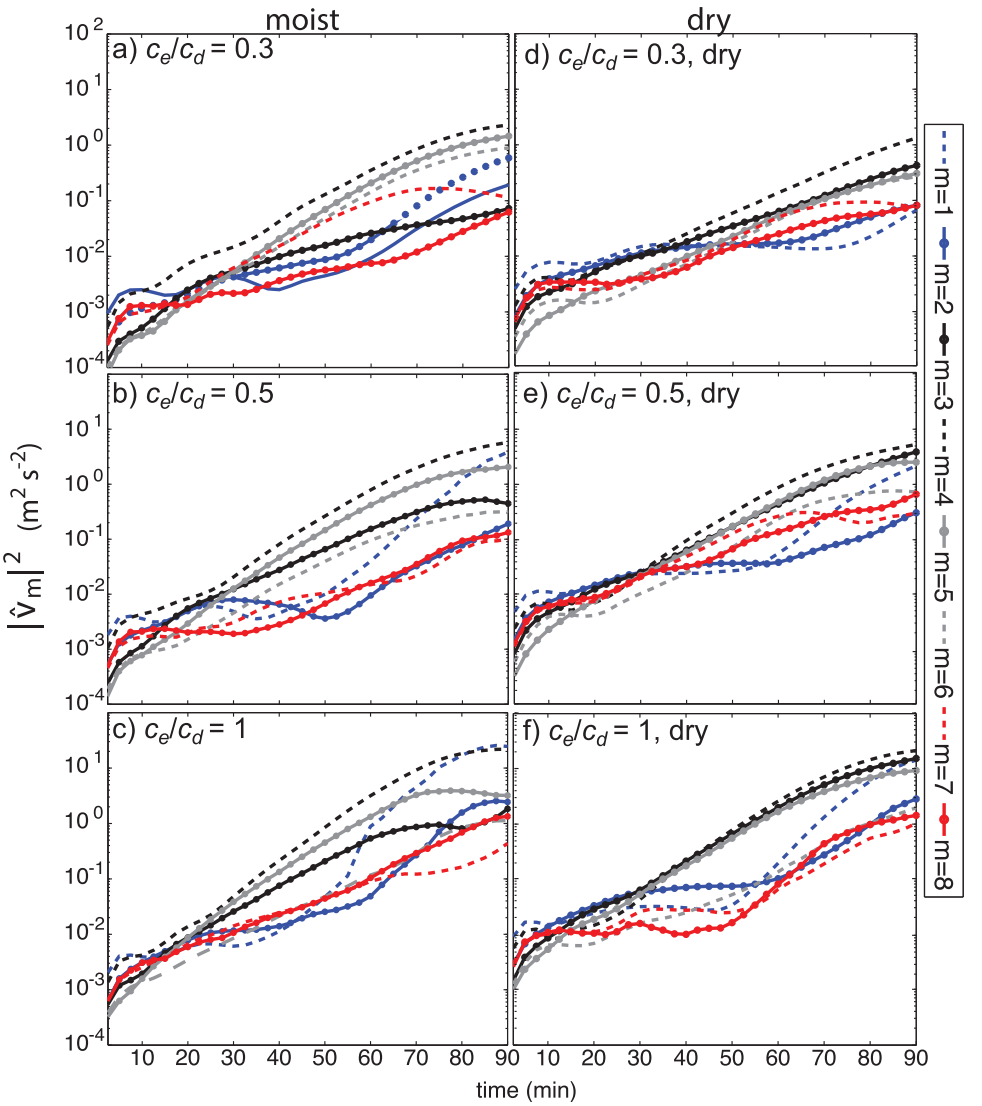

Figure 4. Time series of the squared amplitude of select components from the Fourier expansion of tangential velocity. The squared amplitudes were radially averaged over a 30 km interval centered on the radius of maximum wind (RMW), and vertically averaged from z=0.78 km to z=2.75 km. Moist simulations are in the left plots, and dry simulations in the right.

min is not simply due to differences in perturbation growth rate. At no point in the c_e/c_d=0.3 or c_e/c_d=0.5 simulations is the asymmetry measured by χ as strong and deep as what is shown in Figure 5c.

Figure 6 shows the horizontal structure of ζ at two different levels: z=1.2 km and z=8.75 km. In the c_e/c_d=0.3 simulation (Figures 6a and 6b), asymmetries in upper level ζ are very weak, and the upper level annulus is displaced radially outward from the low-level ζ annulus. In contrast, the simulation with c_e/c_d=0.5 shows some overlap between the low-level and upper level ζ annuli (Figures 6c and 6d). Additionally, at t=90 min (Figure 6c) a somewhat weak polygonal pattern is evident in the upper level ζ annulus that is approximately in phase with the low-level pattern. The small drag simulation (c_e/c_d=1) exhibits even greater overlap between the low and upper level ζ annuli (Figures 6e and 6f). In this simulation, the upper level asymmetry is not only in phase with the low-level asymmetry, but the upper level ζ field shows evidence of strong vorticity roll up. This indicates the presence of deep, coherent mesovortices in the c_e/c_d=1 simulation—a feature not evident in the larger drag simulations.

The vertical extent of the initial instability in each dry simulation (Figure 7) is similar to that seen in its moist counterpart (cf. Figure 5). In the dry c_e/c_d=0.3 simulation, the substantial part of the asymmetry diminishes at approximately z=6 km. The c_e/c_d=0.5 simulation has a moderate asymmetry extending slightly higher,

© 2014. The Authors.

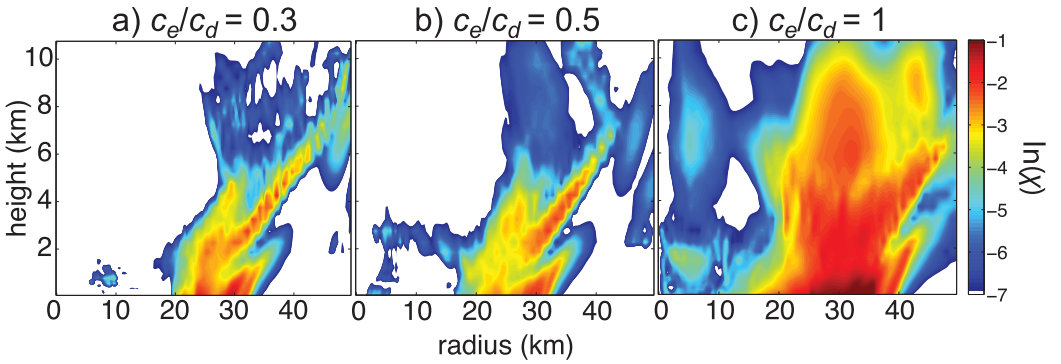

Figure 5. Radial-height structure of the asymmetry parameter χ (see text for a description of this field) at t=90 min for the three moist simulations.

while the c_e/c_d=1 simulation has a strong, deep asymmetry extending up to z=10 km. One notable difference is that the asymmetries in the moist simulations exhibit greater intensity (at 90 min) along the upward and outward sloping inner edge of the eyewall updraft.

3.2.2. Production of Kinetic Energy in the Asymmetric Perturbation

For a more formal investigation into the role of the secondary circulation on the growth of asymmetries, an analysis of perturbation kinetic energy was performed. The kinetic energy per unit mass of the asymmetric perturbation is defined by $KE' = 0.5\left(\overline{u'^2}+\overline{v'^2}+\overline{w'^2}\right)$, in which u, v, and w, respectively, denote the radial, azimuthal, and vertical velocity fields. Overbars represent the azimuthal mean and primed quantities are perturbations from the azimuthal mean. The equation governing the local time tendency of KE' in CM1 can be approximated by

$$\frac{\partial KE'}{\partial t} \approx MFX + EFX + VR + VZ + MSC + PFX + BU + DV, \tag{4}$$

in which

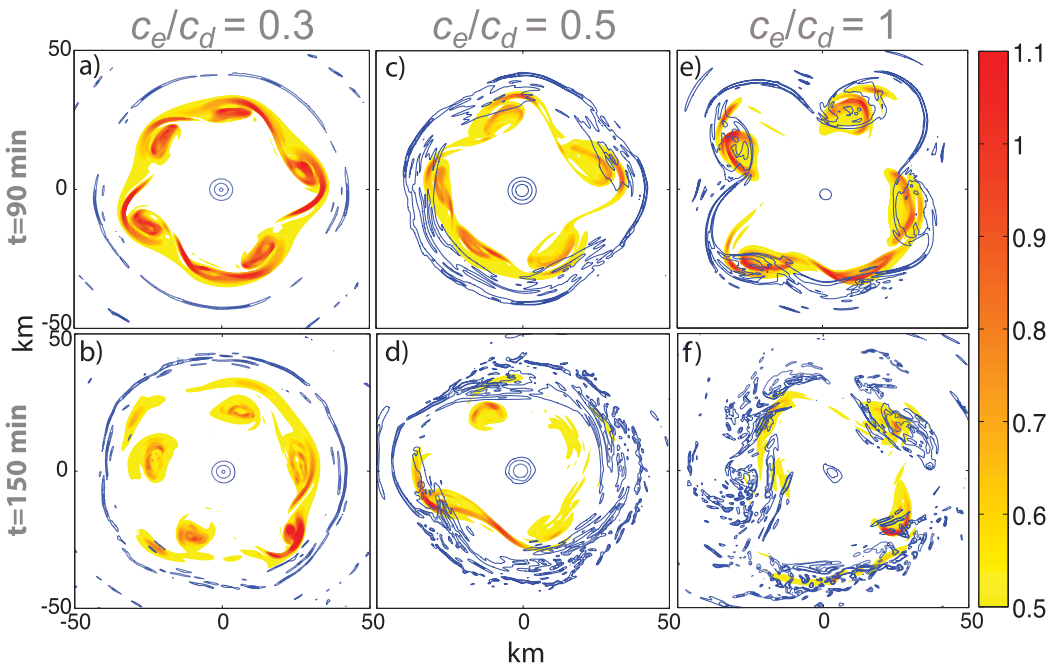

Figure 6. Horizontal cross sections of dimensionless vertical vorticity at z=1.2 km (filled contours) and z=8.75 km (blue contours) in the moist simulations. In each simulation, vertical vorticity at height z was normalized by the maximum value at t=0. The blue contours range from 0.6 to 1.0 with an interval of 0.2.

© 2014. The Authors.

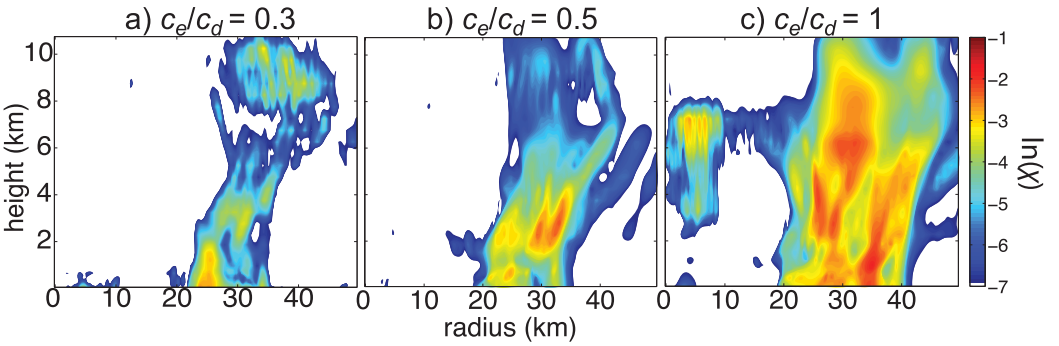

Figure 7. Same as 5, except for the dry 3-D simulations.

$$MFX = -\frac{1}{r}\frac{\partial r\bar{u}KE'}{\partial r} - \frac{\partial \bar{w}KE'}{\partial z}$$

$$EFX = -\frac{1}{r}\frac{\partial r\overline{u'\left(\frac{u'^2}{2}+\frac{v'^2}{2}+\frac{w'^2}{2}\right)}}{\partial r} - \frac{\partial \overline{w'\left(\frac{u'^2}{2}+\frac{v'^2}{2}+\frac{w'^2}{2}\right)}}{\partial z}$$

$$VR = -r\frac{\partial}{\partial r}\left(\frac{\bar{v}}{r}\right)\overline{u'v'},$$

$$VZ = -\frac{\partial \bar{v}}{\partial z}\overline{v'w'},$$

$$MSC = -\frac{\partial \bar{u}}{\partial r}\overline{u'^2} - \frac{\partial \bar{u}}{\partial z}\overline{u'w'} - \frac{\partial \bar{w}}{\partial r}\overline{u'w'} - \frac{\partial \bar{w}}{\partial z}\overline{w'^2} - \bar{u}\frac{\overline{v'^2}}{r},$$

$$PFX = -C_p\bar{\theta}_\rho\left(\overline{u'\frac{\partial \Pi'}{\partial r}} + \overline{\frac{v'}{r}\frac{\partial \Pi'}{\partial \lambda}} + \overline{w'\frac{\partial \Pi'}{\partial z}}\right)$$

$$BU = \frac{g}{\theta_{\rho 0}}\overline{w'\theta'_\rho},$$

$$DV = \overline{u'D'_r} + \overline{v'D'_\lambda} + \overline{w'D'_z}.$$

In the preceding definitions, C_p is the specific heat of dry air at constant pressure, θ_ρ is density potential temperature, $\theta_{\rho 0}(z)$ is the base state of θ_ρ, Π is the Exner function, g is gravitational acceleration, and D is the subgrid velocity tendency in the radial (r), azimuthal (λ), and vertical (z) directions. *MFX* and *EFX* are flux convergences of perturbation kinetic energy attributable to the mean flow and eddies. *VR* and *VZ* account for the production of KE' due the radial and vertical shear of the mean azimuthal flow. *MSC* is the production rate of KE' due to the mean secondary circulation. *PFX* is related to the local work done by the

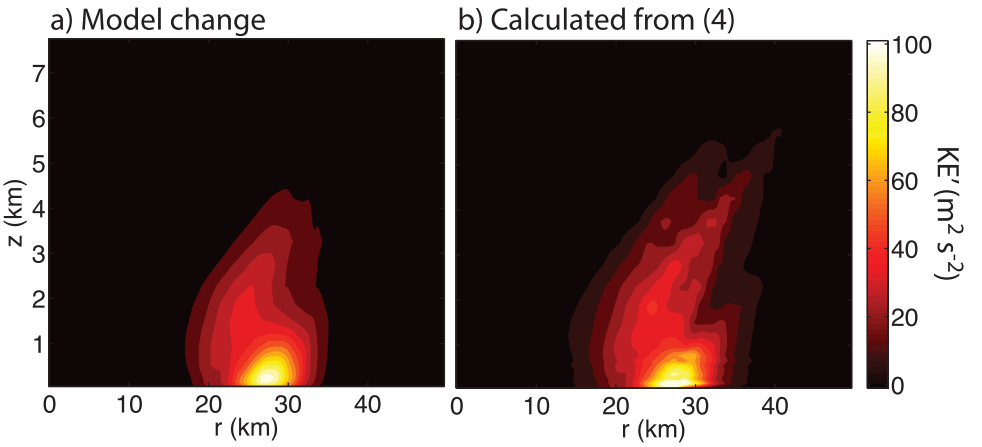

Figure 8. Comparison of total change in eddy kinetic energy from t=30 min to t=90 min calculated via (a) the difference in KE' between model history files at these times and (b) the time integral of all terms on the RHS of (4) obtained from history files generated every 2.5 min. Results shown here are from the moist simulation with $c_e/c_d = 0.3$.

© 2014. The Authors.

Table 1. KE' Produced by Each Term in the Eddy Kinetic Energy Equation, Expressed as a Percentage of the Total KE' Produced by the Positive Source Terms[a]

	Moist			Dry		
	$c_e/c_d=0.3$	$c_e/c_d=0.5$	$c_e/c_d=1$	$c_e/c_d=0.3$	$c_e/c_d=0.5$	$c_e/c_d=1$
MFX	0.08	0.22	0.01	−0.01	−0.04	−0.04
EFX	0.02	0.04	0.16	−0.01	−0.10	−0.11
VR	88.34	92.09	92.80	90.07	90.14	89.41
VZ	−6.89	−7.08	−5.53	0.66	−1.15	−10.85
MSC	4.69	2.09	2.55	3.65	0.26	−0.10
PFX	5.77	5.55	4.49	5.62	9.60	10.59
BU	1.06	−8.75	−11.77	−15.72	−19.93	−15.99
DV	−27.53	−21.52	−16.70	−0.17	−0.094	−0.03
Error	7.9	3.3	−1.9	15.7	5.8	4.2

[a]The tabulated values correspond to integrals of the source terms over the cylindrical volume defined by $0 \leq r \leq 80$ km and $0 \leq z \leq 15$ km, and over the time interval from $t=30$ min to $t=90$ min. The error represents the difference between the integrated sum of terms on the RHS of (4) and the integrated tendency of KE' obtained directly from the model. Positive error values indicate that the sum of terms is greater than the model calculated tendency of KE'.

perturbation pressure gradient. *BU* is the production rate of KE' due to buoyancy, and *DV* accounts for subgrid turbulent dissipation. Corrections associated with the 3-D divergence of the velocity field and all KE' production terms involving θ'_ρ—except the *BU* term—are neglected. The mean and perturbation fields are evaluated in a vortex-centered coordinate system that is stationary during the analysis period.

To confirm that (4) is reasonably accurate, the sum of the terms on the right-hand side (RHS) was compared to the model-observed tendency in KE'. Both the terms in (4) and the model-observed tendency were integrated from $t=30$ min to $t=90$ min. Good agreement was found between the two calculations (Figure 8),

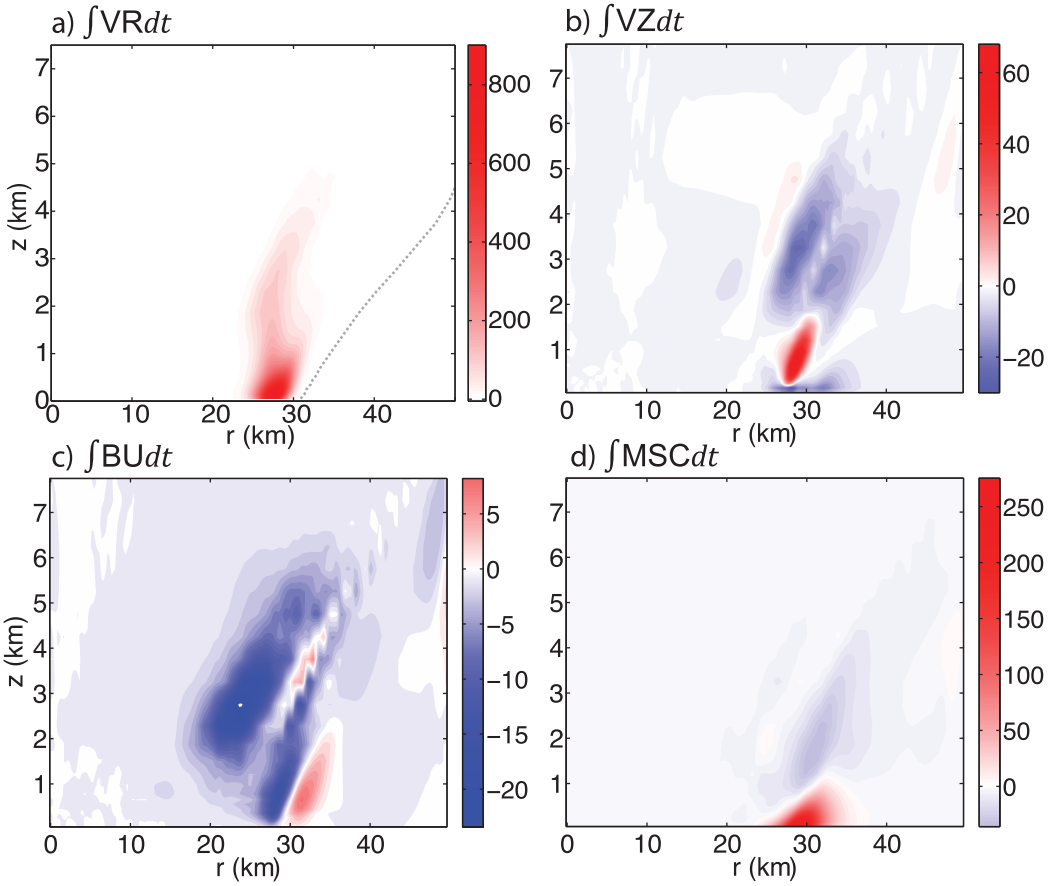

Figure 9. Production terms of eddy kinetic energy from the $c_e/c_d=0.3$ simulation integrated from $t=30$ min to $t=90$ min. The dotted line in (a) is the height-dependent radius of maximum wind. A description of the terms shown in (a–d) is given in the text. Units are $m^2\ s^{-2}$.

© 2014. The Authors.

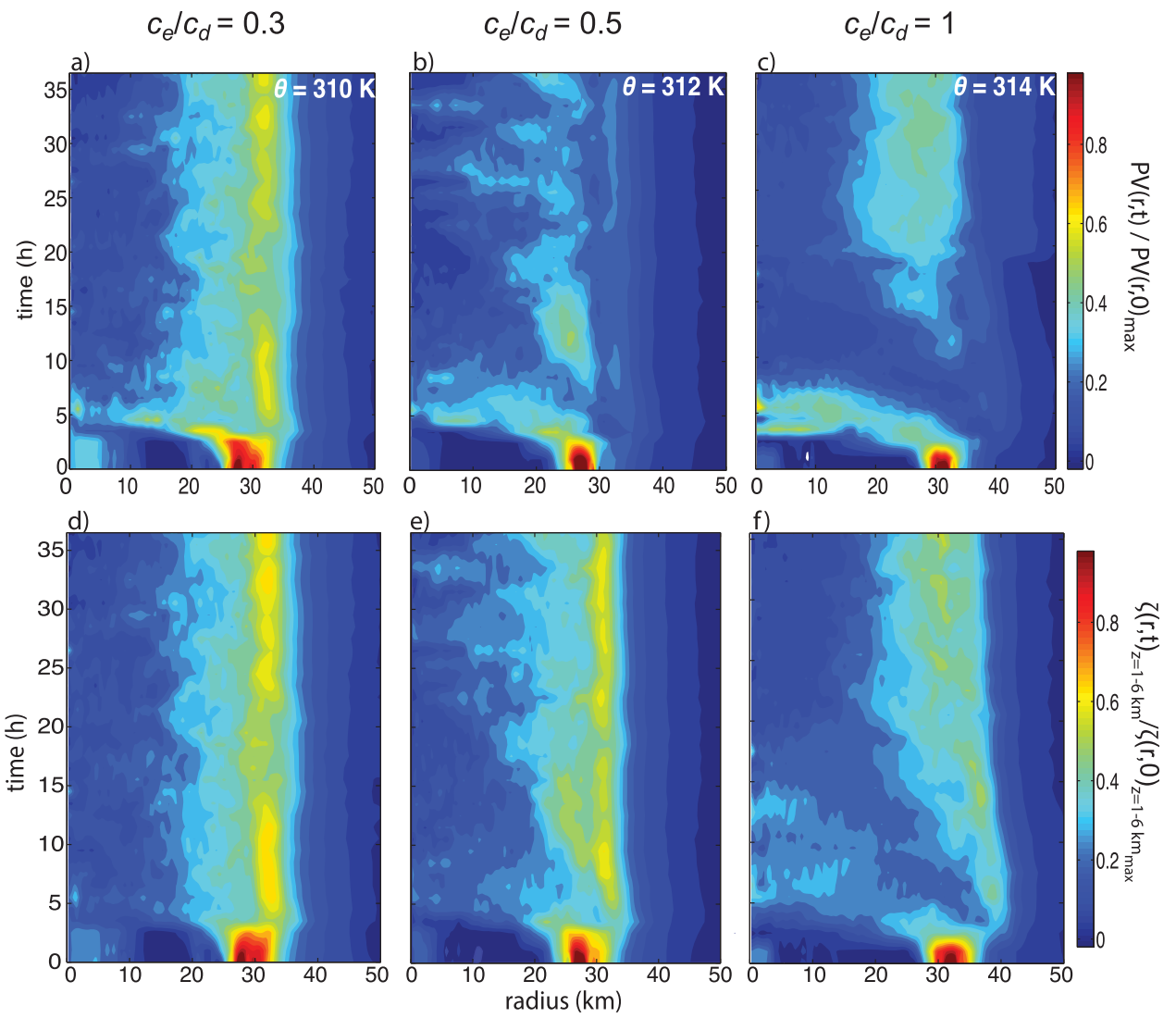

Figure 10. Hovmöller diagrams from the three moist simulations showing: (a)–(c) dimensionless potential vorticity. Values have been normalized by the maximum value at $t=0$ in each simulation. The level of analysis is denoted in the top right corner of each panel. (d)–(f) dimensionless depth-averaged vertical vorticity. Values are averaged from $z=1$ km to $z=6$ km and normalized by the maximum value at $t=0$.

with the greatest differences occurring below $z=0.5$ km. Below this level, the error can be as large as 30%. Above $z=0.5$ km, the error is typically less than 15%.

Table 1 shows the contribution of each source term to the growth of KE' for each simulated vortex. These contributions were obtained by integrating each term in (4) over the cylindrical volume defined by $0 \leq r \leq 80$ km and $0 \leq z \leq 15$ km, and over the time interval from $t=30$ min to $t=90$ min. In all simulations, the *VR* term is by far the dominant source of KE' production. This term contributes roughly 90% of the total positive production of KE', where total positive production is the sum of positive source-term integrals only. The second and third largest sources are *PFX* and *MSC*, respectively. Each of these terms contributes 6% or less of the total positive production of KE' in the moist simulations, and less than 11% in the dry simulations. The primary sink of KE' in the moist simulations is *DV*, while *BU* is the dominant sink in the dry simulations. The relative insignificance of the *DV* term in the dry simulations is likely connected to the elimination of surface drag and the reduction of mixing lengths in the subgrid turbulence parameterization discussed in section 2. In all simulations except the dry $c_e/c_d=0.3$ simulation, the *VZ* term acts as a net sink for KE'.

Figure 9 shows the spatial distribution of select time-integrated KE' production terms from the moist $c_e/c_d=0.3$ simulation. The *VR* term is strongly positive just inside the RMW, with large positive values extending upward to

© 2014. The Authors.

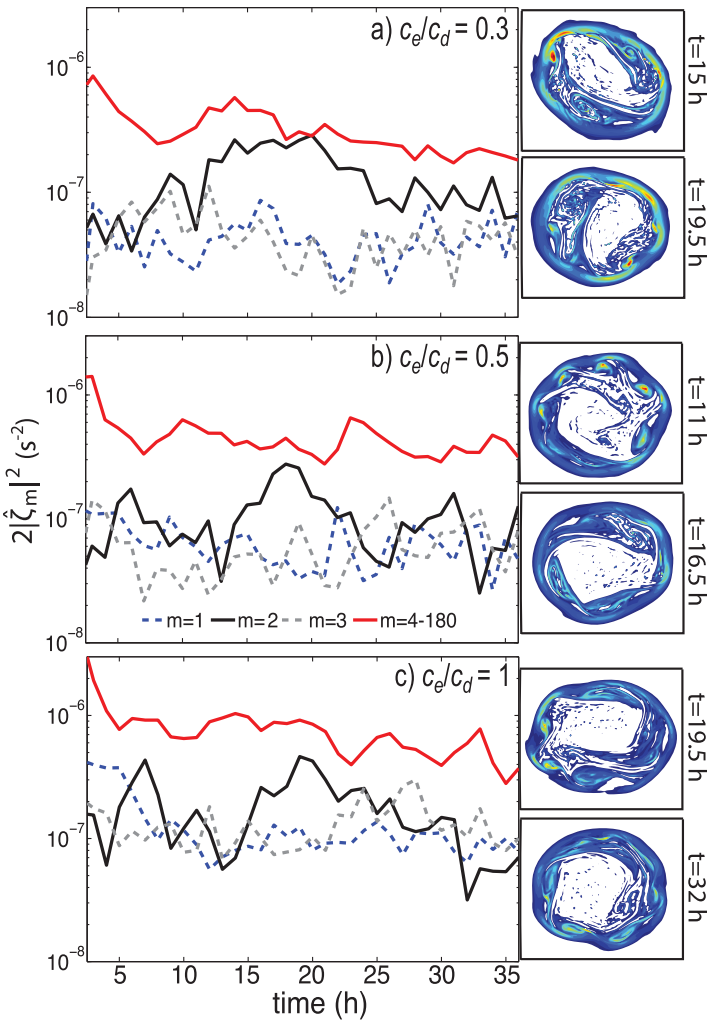

Figure 11. Similar to the left plots of 4, but with the vorticity transform $\hat{\zeta}_m$ replacing $\hat{v}_m$ and the time frame spanning from t=1.5 h to t=36 h. The red curves represent the sum $2\sum_{m=4}^{179}|\hat{\zeta}_m|^2+|\hat{\zeta}_{180}|^2$. Also shown are select snapshots of dimensionless vertical vorticity at z=1.2 km. The color scale is the same as in Figure 3.

approximately z=4 km (Figure 9a). The *VZ* term is maximized just inside the RMW at approximately z=1 km, but the maximum magnitude is more than 10 times smaller than the *VR* term (Figure 9b). The *BU* term is also weak compared to the *VR* term (Figure 9c). The *MSC* term has large positive values near the RMW, with the values being concentrated below z=1 km (Figure 9d). The maximum of *MSC* is 3 times less than the maximum of *VR*. In other words, the early production of *KE*′ comes mostly from the radial shear of mean angular velocity, while production from the secondary circulation seems to be less important. The preceding results contrast those of *Nolan* [2012], who found that vertical shear of mean angular velocity and radial shear of $\bar{w}$ can be strong contributors to the development of *KE*′ in tornado-like vortices.

3.3. Long-Term Evolution of PV and Vertical Vorticity

The results shown thus far suggest that moist convection does not profoundly affect the early growth of inner core asymmetries. The same cannot be said for the effect of moist convection on the long term evolution of the system. This subsection describes how the PV and ζ distributions evolve differently in the moist and dry simulations.

Figures 10a–10c show *r-t* Hovmöller plots of azimuthally averaged PV on select isentropic surfaces in the moist simulations. The PV is here defined by $(\overrightarrow{\omega_a}\cdot\nabla\theta)/\rho$, in which ρ is mass density and $\overrightarrow{\omega_a}$ is the absolute vorticity vector. The θ-levels chosen for these plots correspond to heights near z=1.5 km above the strong radial inflow but within the layer of strong asymmetric development [cf. Figures 5 and 8]. Following the initial growth of asymmetries, each simulation shows evidence of PV transport from the eyewall deep into the eye. Such "mixing" is a nonlinear and chaotic process that usually involves merger of mesovortices and vigorous stirring of the surrounding fluid. In all cases, the time scale for PV mixing following the instability is approximately 5–10 h. Subsequently, the central PV dissipates and the PV ring reintensifies. It seems reasonable to speculate that the dissipation of central PV involves both diabatic and frictional processes, but a thorough analysis is deferred to a separate study. The restored PV ring generally appears weaker and broader than the original ring. This structural change is partly due to persistent asymmetries that will be discussed shortly.

While a common pattern is seen in the evolution of PV among the moist simulations, there is clearly variation in details. The simulation with the weakest drag exhibits the most dramatic deterioration and slowest restoration of the azimuthally averaged PV ring (Figure 10c). Another distinction at small drag can be seen

© 2014. The Authors.

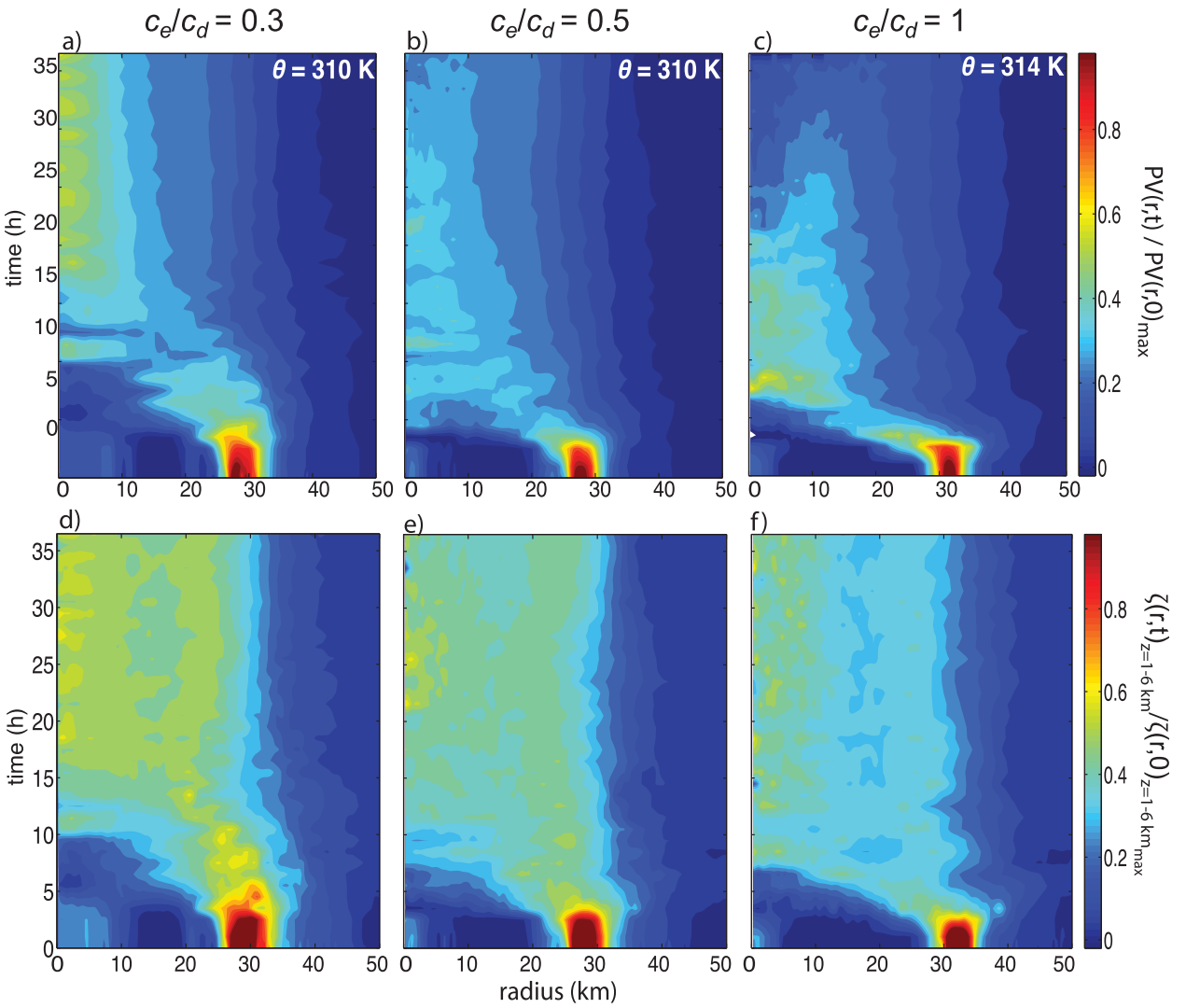

Figure 12. Same as 10, except for the dry simulations.

in Hovmöller plots of the symmetric vertical vorticity distribution, averaged between $z = 1$ and $z = 6$ km (Figures 10d–10f). The ζ-plot for $c_e/c_d = 1$ shows the strongest growth of inner vorticity during the primary mixing event. This seems to partly reflect greater inward transport of ζ.

Figure 11 depicts the evolving spectral composition of the asymmetric vertical vorticity perturbation in the broad vicinity of the RMW of each moist vortex. After the initial mixing event of the simulation with $c_e/c_d = 0.3$, a strong elliptical (m=2) asymmetry emerges that is momentarily comparable to the combined asymmetry of wavenumbers 4–180. For $c_e/c_d = 0.5$ and $c_e/c_d = 1$, the high wave number contribution to the vorticity perturbation substantially exceeds the individual contribution from the elliptical mode for all $t \geq 1.5$ h. Transient peaks in the high wave number contribution are usually connected to the emergence of prominent mesovortices.

The evolutions of PV and ζ in the moist simulations are in stark contrast to what occurs in the dry simulations. Figure 12 illustrates the permanent development of monotonic radial distributions of vertical vorticity following the initial instabilities of the dry vortices. Unlike their moist counterparts, the dry vortices have no mechanism to regenerate an off-center vorticity annulus. A slightly off-center maximum reemerges in one of the PV Hovmöller plots only because the peak of the PV distribution at the corresponding θ-level temporarily moves away from the coordinate center. Figure 13 demonstrates that the dry vortices generally relax to elliptical structures with well-mixed interiors.

© 2014. The Authors.

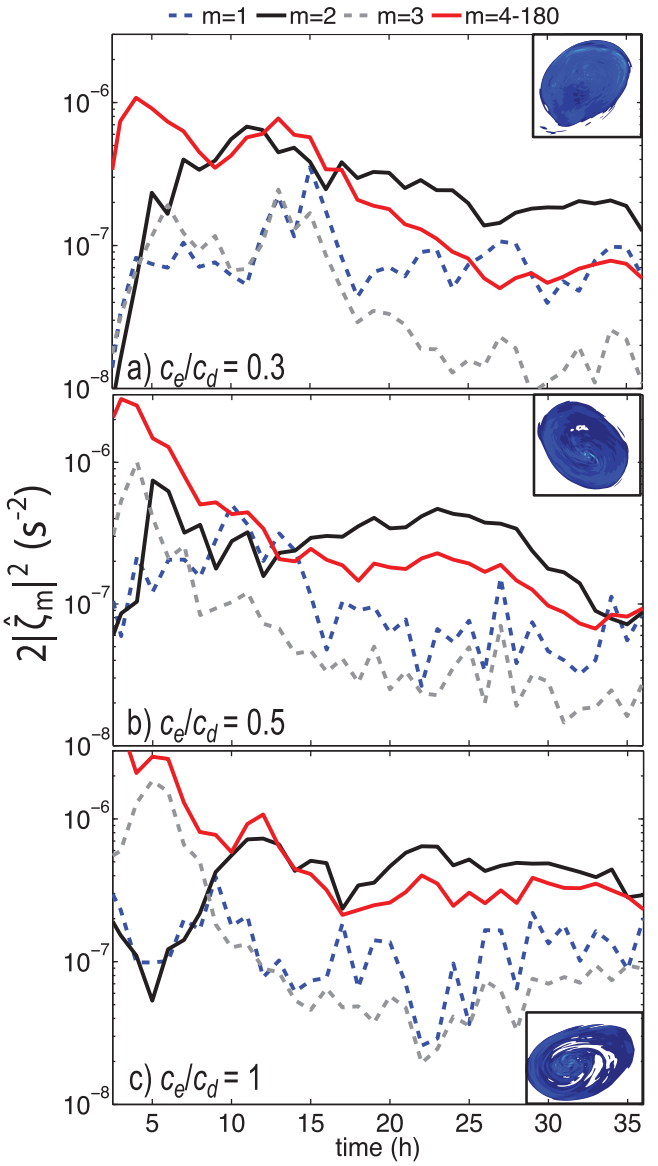

Figure 13. Same as 11, except for the dry simulations. Insets are horizontal cross sections of dimensionless vertical vorticity at $t=20$ h.

At this point, the reader is reminded that the moist and dry simulations have different settings in the subgrid turbulence parameterization. The vertical and horizontal mixing coefficients (K) are O[100 $m^2\ s^{-1}$] in the moist simulations versus O[1 $m^2\ s^{-1}$] in the dry simulations. The dissipation associated with either magnitude of K is estimated to have little impact during the initial wave growth period of the instability [cf. Table 1]. On the other hand, the larger magnitude of K in the moist simulations may allow the subgrid turbulence parameterization to more substantially affect how the PV and ζ distributions evolve during and after the primary mixing event [e.g., *Zhu et al.*, 2013; *Schecter et al.*, 1999].

3.4. Evolution of Intensity

In all simulations (both moist and dry), a sharp increase in maximum 10 m wind speed occurs around $t=1$ h—coinciding with the development of eyewall mesovortices (Figure 14). The relative increase in wind speed is larger in the moist simulations than in the dry. It is conceivable that vortex stretching by convection helps amplify the moist signal. The duration of the increase varies greatly between the three moist simulations and appears to be a function of c_d. In the $c_e/c_d=1$ case, the initial spike in maximum 10 m wind speed lasts less than 2 h, whereas the spike in the $c_e/c_d=0.3$ simulation does not subside until after $t=5$ h. Following this spike, 10 m wind speeds in the $c_e/c_d=0.3$ and $c_e/c_d=0.5$ simulations remain slightly stronger than their original values for the next 8–10 h, while the maximum in the $c_e/c_d=1$ simulation drops 5–7%. However, by the end of the 36 h simulation, the maximum 10 m wind speed in all three simulations is approximately the same as the initial conditions. In contrast, the maximum wind in the dry simulations steadily decreases, with an overall reduction of 5–10% by the end of the simulations.

The early evolutions of maximum azimuthally averaged tangential velocity ($\overline{v}_{max}$) in the dry and moist simulations are also similar (Figure 15). After the first hour of simulation, during the time period of the initial PV mixing event, $\overline{v}_{max}$ begins to decrease in all simulations, with the most rapid decrease occurring in the $c_e/c_d = 1$ simulation. During this time, the rate of change in $\overline{v}_{max}$ is similar in each moist simulation and its dry analog. However, by $t \approx 5$ h, the dry and moist simulations begin to diverge. In the dry simulations, $\overline{v}_{max}$ continues to decrease while in the moist simulations $\overline{v}_{max}$ reaches a local minimum and begins to increase.

© 2014. The Authors.

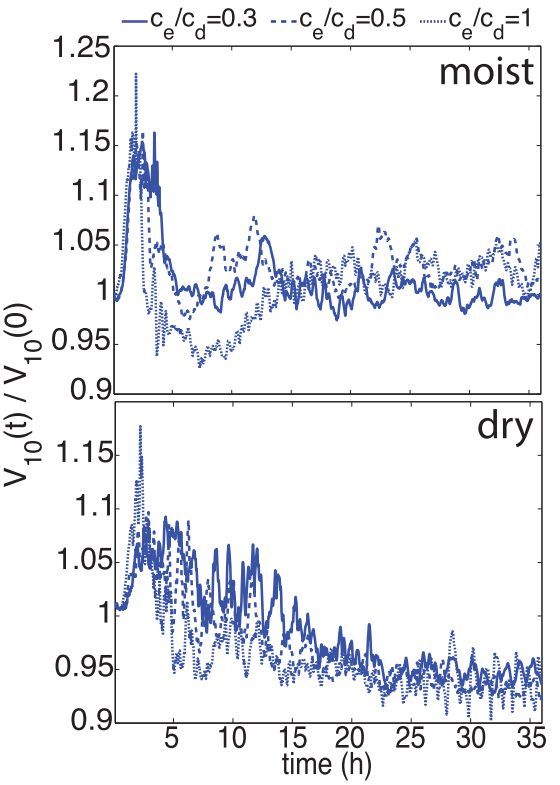

Figure 14. Time series of maximum 10 m horizontal wind speed, normalized by the maximum value at $t=0$, for the moist (top) and dry (bottom) simulations.

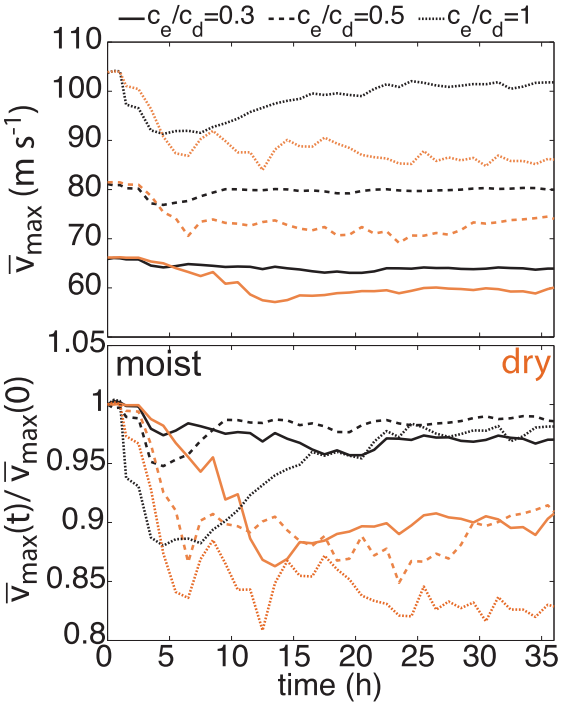

Figure 15. Time series of maximum azimuthally averaged tangential velocity for the moist (black lines) and dry (orange lines) simulations. The top plot shows the dimensional tangential velocity, whereas the bottom plot shows the tangential velocity normalized by the maximum value at $t=0$.

In the moist simulations, the change in $\overline{v}_{max}$ is related to the magnitude of c_d. The $c_e/c_d=1$ case is the only moist simulation to produce a substantial decrease in $\overline{v}_{max}$ (about 13% decrease by $t=10$ h). However, this weakening is relatively short lived. By 36 h in each moist simulation, $\overline{v}_{max}$ returns to within 4 percent of its initial value, while the dry simulations see a decrease in $\overline{v}_{max}$ of approximately 9–17%.

In an analysis modeled after that of *Persing et al.* [2013], the impact of asymmetries on the evolution of the primary circulation was investigated by examining terms from the azimuthally averaged tangential velocity equation,

$$\frac{\partial \bar{v}}{\partial t} \approx -\bar{u}\overline{(f+\zeta)} - \bar{w}\frac{\partial \bar{v}}{\partial z} - \overline{u'\zeta'} - \overline{w'\frac{\partial v'}{\partial z}} + \bar{D}_{\lambda}. \quad (5)$$

As before, variables with overbars denote azimuthal mean values and primed quantities are perturbations from the azimuthal mean. The first two terms on the RHS of (5) are connected to angular momentum transport by the mean flow, while the next two terms account for eddy transport. The last term is the tendency associated with subgrid turbulence. Note that (5) neglects the term $-(C_p/r)\overline{\theta'_{\rho}\partial\Pi'/\partial\lambda}$. Testing has revealed that this term is relatively small and can be ignored.

A time-average (over the first 90 min of simulation) of all terms in (5) is shown in Figure 16. In all three moist cases, the low-level positive tendency from the mean terms (Figures 16a, 16e, and 16i) is countered by a comparable negative tendency in the subgrid terms (Figures 16c, 16g, and 16k). The eddy terms (Figures 16b, 16f, and 16j) act to decrease $\overline{v}$ at the RMW and increase $\overline{v}$ inside the RMW at low levels. The total tendency computed by CM1 shows that $\overline{v}$ is increasing inside the RMW while decreasing at the RMW in all three simulations (Figures 16d,

© 2014. The Authors.

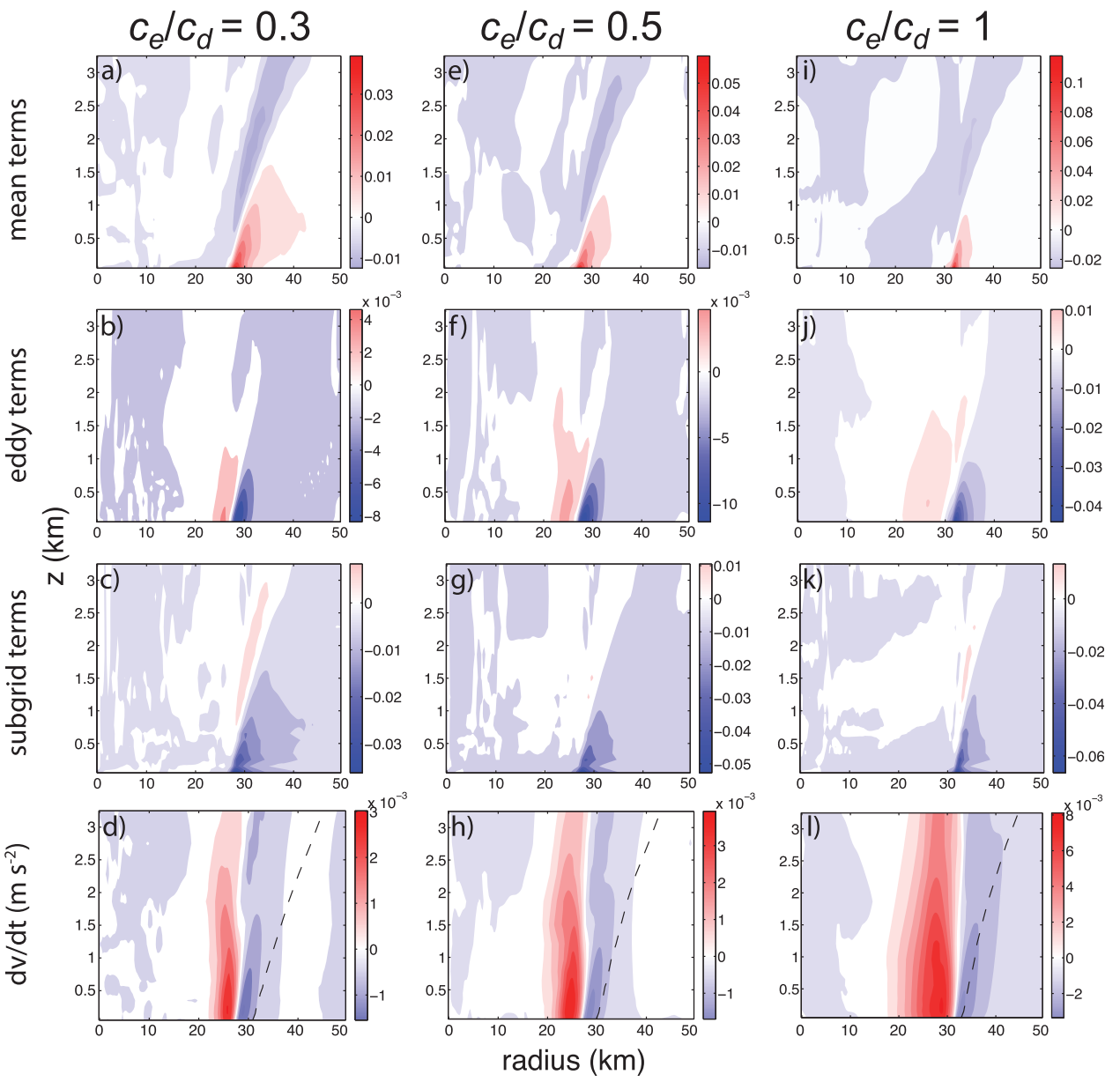

Figure 16. Height-radius plots of tendency terms in the azimuthally averaged tangential velocity equation for the moist 3-D simulations. Terms are averages from $t=0$ to $t=90$ min. The mean terms (top row) represent the sum of the first two terms on the RHS of (5), the eddy terms (second row) represent the sum of the third and fourth terms on the RHS of (5), and the bottom row shows the model simulated tendency in $\bar{v}$. The dashed line in the bottom plots is the height-dependent radius of maximum wind. Units are m s^{-2}.

16h, and 16l). Note that this tendency is in reasonable agreement with the RHS of (5) away from the eyewall updraft, but some discrepancies are found to exist where the mean secondary circulation is relatively strong. In the latter region, low-order finite differencing used for analysis (in contrast to high-order finite differencing used by CM1) does not seem sufficiently accurate to compute small residuals of large terms with opposite signs.

Figure 17 further illustrates how the radial profile of $\bar{v}$ changes between $t = 0$ and 90 min. The radial profiles are taken along the contour $z = z_{max}(r)$, in which z_{max} is the altitude where $\bar{v}$ is maximized with respect to variation in z. In all three simulations, $\bar{v}(r, z_{max})$ at the original RMW decreases with time, while winds inside the RMW increase with time. The evolution illustrates how barotropic instability can smooth sharp gradients in $\bar{v}$ that might otherwise develop in the boundary layer [cf. *Williams et al.*, 2013].

© 2014. The Authors.

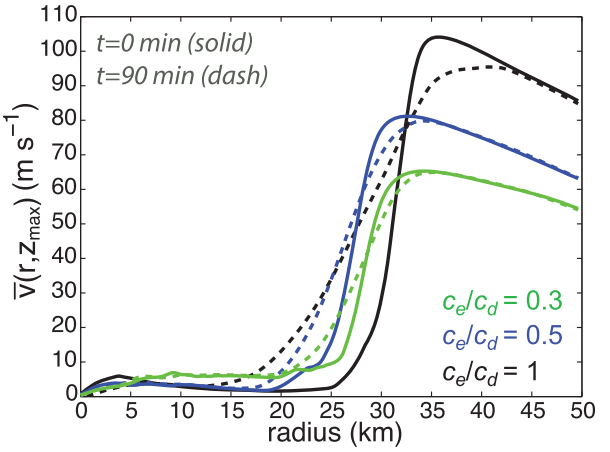

Figure 17. Radial profiles of the azimuthally averaged tangential velocity ($\bar{v}$) taken at the level of maximum $\bar{v}$ from the moist 3-D simulations at $t=0$ (solid lines) and $t=90$ min (dashed lines).

Figure 15 suggests that each moist TC returns to a quasi steady state by the end of the simulation period. It is of interest to see how the instability changed local parameters that theoretically determine the maximum wind speed of the steady state primary circulation. In theory, the squared maximum wind speed of a steady state TC with weak (formally negligible) asymmetry satisfies the following equation:

$$\bar{v}^2_{max} = EPI^2 + \Gamma \equiv PI^2_+, \tag{6}$$

in which

$$EPI^2 = \frac{T_s}{T_o}\left[\frac{c_e}{c_d}(T_b - T_o)(s_{sfc} - s_0)\right] \text{ and}$$

$$\Gamma = \frac{T_s}{T_o}[r_b \eta_b w_b]. \tag{7}$$

Here, T_s is the sea surface temperature, T_o is the outflow temperature, T_b is the temperature at the top of the boundary layer, s_{sfc} is the saturated moist entropy at the sea surface, s_0 is the moist entropy at the top of the surface layer, w_b is vertical velocity, and η_b is azimuthal vorticity [*Bryan and Rotunno*, 2009]. All terms in (7) are azimuthal averages (or constants). Terms with a *b* subscript are evaluated at the *r*, *z* location of $\bar{v}_{max}$. Entropies are evaluated at the RMW and are calculated using the approximate pseudoadiabatic formula from *Bryan* [2008]. T_o is here approximated by the initial ambient temperature at the level of maximum $\bar{u}$ in the outflow layer. Because the RHS of (6) depends on local vortex parameters, it is not a closed theory for the maximum potential wind speed of the TC. The notation PI_+ ("potential intensity plus") is nevertheless used to be somewhat consistent with *Bryan and Rotunno* [2009]. The EPI^2 component of PI^2_+ is the square of the theoretical wind speed of a TC that satisfies gradient and hydrostatic balance [e.g., *Emanuel*, 1995]. The Γ component is due to unbalanced flow.

Yang et al. [2007] concluded that asymmetries resulting from barotropic instability decreased *EPI* (and therefore $\bar{v}_{max}$) in their simulated hurricane by decreasing updraft tilt, and thereby weakening downdrafts that would otherwise maintain a relatively large entropy deficit at the air-sea interface. A similar conclusion cannot be made for the present simulations. Here, updraft tilt appears to be unaffected during the 36 h run time (not shown). Moreover, there is very little change in EPI^2. Figure 18 shows the 36 h changes in PI^2_+, EPI^2, and Γ next to the 36 h changes in $\bar{v}^2_{max}$. The change of EPI^2 is slightly positive in all three moist simulations whereas the change in Γ is slightly negative [cf. *Schecter*, 2013]. These trends were confirmed out to 54 h in an extended simulation with $c_e/c_d = 1$. Note that the small changes in $\bar{v}^2_{max}$ do not generally agree with the corresponding changes in PI^2_+. In other words, the subtle weakening of TCs in the present simulations may involve subtle processes that are neglected in the derivation of (6).

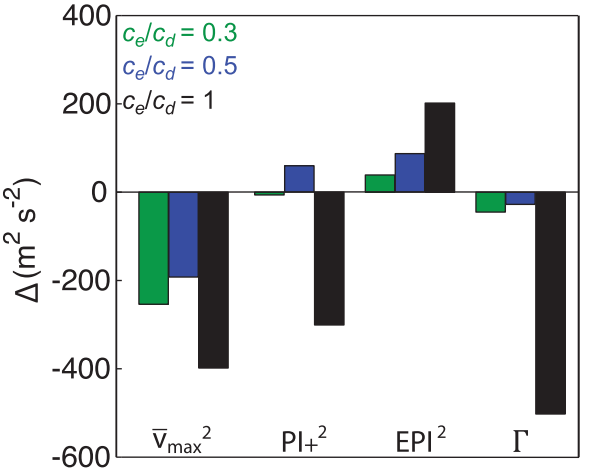

Figure 18. Change in $\bar{v}_{max}{}^2$, PI^2_+, EPI^2, and Γ between $t=0$ and $t=36$ h.

3.5. Precipitation

It is reasonable to assume that the development of inner core asymmetries influences the pattern and intensity of precipitation. In this section, the evolution of rain band

© 2014. The Authors.

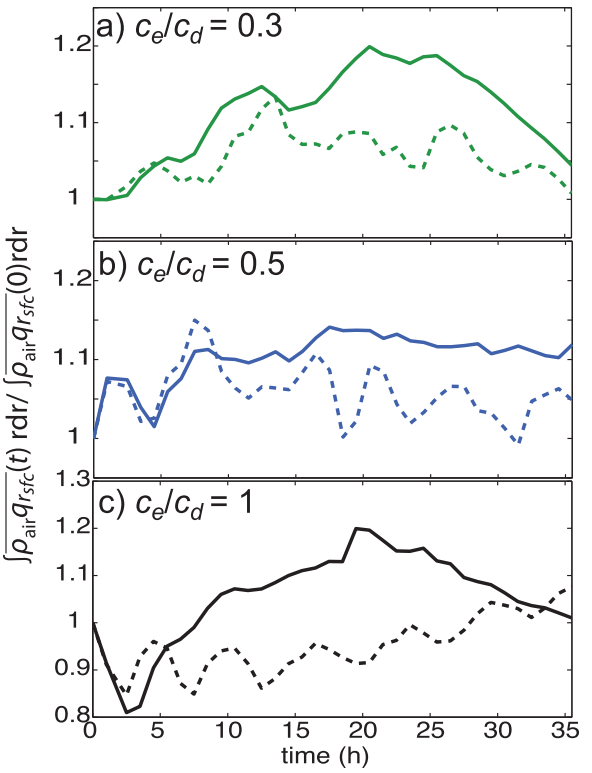

Figure 19. Time series of integrated surface rainwater density from the moist 3-D simulations (solid lines). Dashed lines show the surface rain mass from axisymmetric simulations initialized with the same initial vortex used in the 3-D simulations. The integration limits are r=0 and r=100 km. Rainwater density is defined as the product of rain water mixing ratio (q_r) and dry air density (ρ_{air}).

activity and total surface rainwater in the moist simulations is examined.

Figure 19 shows the time evolution of surface rainwater density integrated over the area within a 100 km radius of the vortex center. During the first few hours of run time, surface rainwater decreases in all three moist simulations. After this time, all simulations show an increase in surface rainwater. In general, the peak in surface rainwater occurs between t=20 h and t=30 h and is at least 1.1 times greater than the value at t=0. To help determine if the increase in rainwater is related to asymmetric processes, the dashed lines in Figure 19 show the results from moist axisymmetric simulations whose initial conditions equal those of the 3-D simulations. In each axisymmetric simulation, the maximum change in surface rainwater is less than the corresponding change in its 3-D counterpart. For c_e/c_d=0.3 and c_e/c_d=1, the maximum change in the axisymmetric simulation is about half of the change that occurs in the 3-D simulation. In the 3-D simulations with c_e/c_d=0.3 and c_e/c_d=1, the increase in total surface rainwater coincides with increasing precipitation at radii greater than 60 km (Figure 20). In contrast, the c_e/c_d=0.5 simulation—which experiences a smaller increase in total rainwater—does

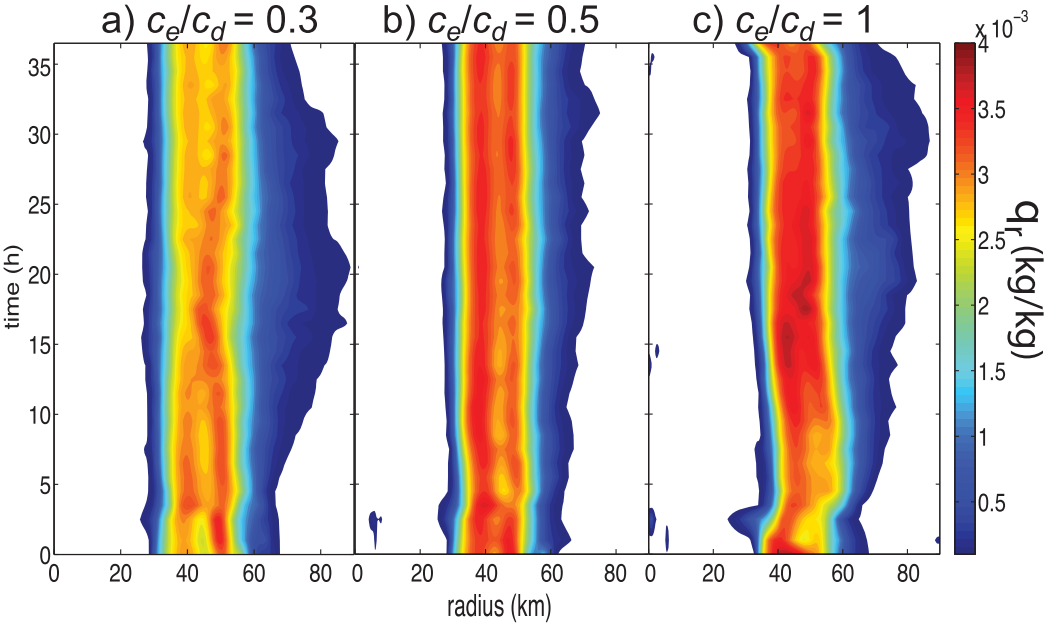

Figure 20. Hovmöller diagrams of azimuthally averaged surface rainwater mixing ratio in the moist simulations.

© 2014. The Authors.

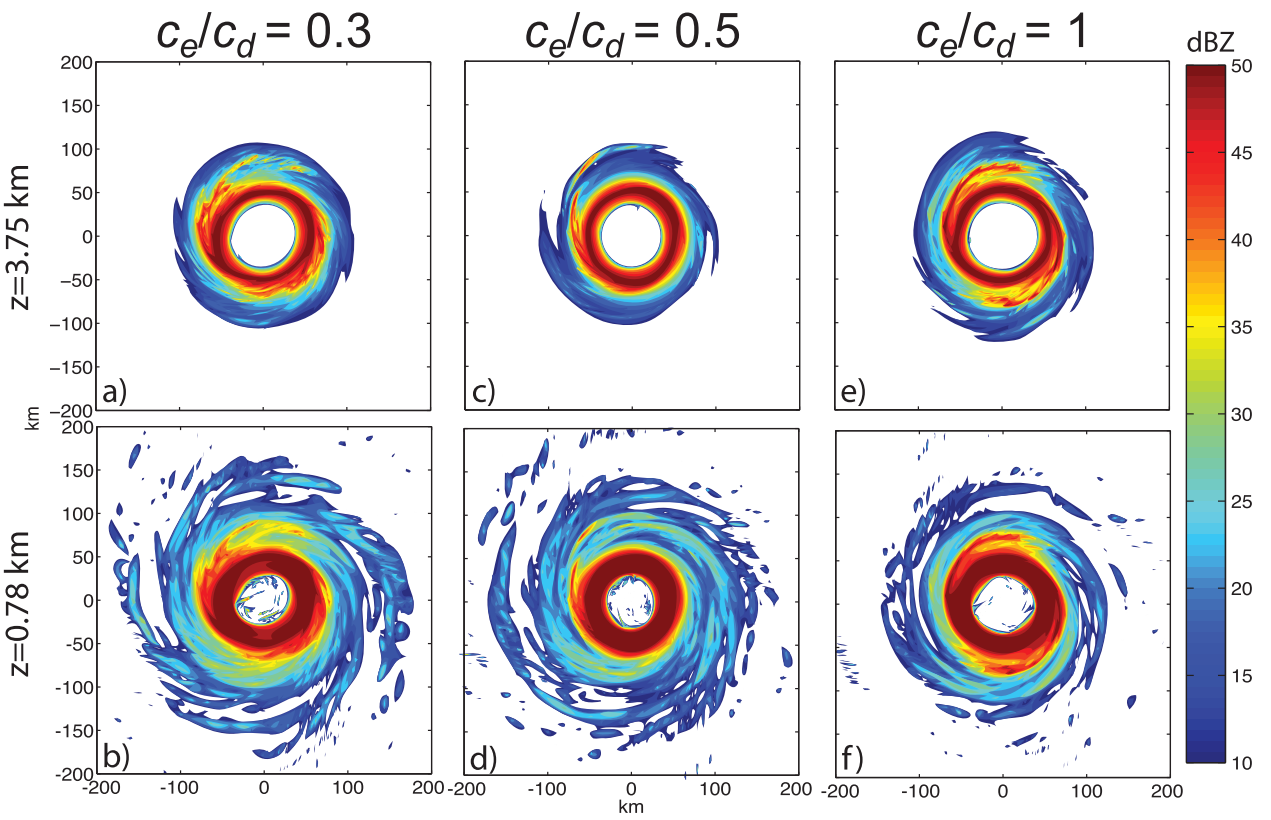

Figure 21. Horizontal cross sections of simulated radar reflectivity at $t=20$ h in the moist simulations. The calculation of radar reflectivity follows that of *Smith et al.* [1975].

not produce much rainwater beyond a radius of 60 km at any point in the simulation, nor are there strong fluctuations in the eyewall convection.

The spatial distribution of the convection at $t=20$ h is shown in Figure 21. The outermost bands are composed of shallow convection, as they are not visible in plots at $z=3.75$ km (Figures 21a, 21c, and 21e). These shallow outer bands occur at radii greater than 100 km and do not have a strong influence on the total surface rainwater (Figure 19). Both the $c_e/c_d=0.3$ and $c_e/c_d=1$ simulations possess prominent and persistent inner rain bands between $r=50$ km and $r=100$ km. These inner bands have a simulated reflectivity of greater than 35 dBZ and seem largely responsible for the increase in total surface rainwater in these simulations. In contrast, the $c_e/c_d=0.5$ simulation does not exhibit the same inner rain band structure, which likely explains why this simulation does not show as large of an increase in total surface rainwater. Thus, it appears as if asymmetric processes associated with rain bands are acting to slightly increase the total surface precipitation in the 3-D simulations.

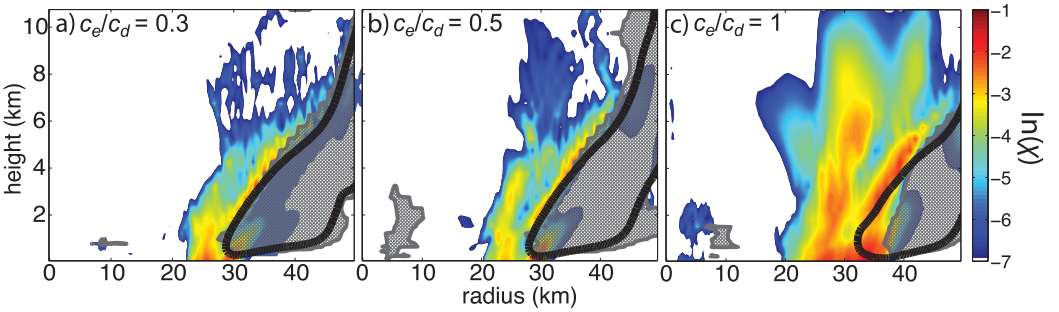

Figure 22. Height-radius plots of the asymmetry variable χ at $t=75$ min for the moist simulations. The thick black contour is the 1 m s^{-1} vertical velocity contour and the gray hatched area is relative humidity greater than 99 percent.

© 2014. The Authors.

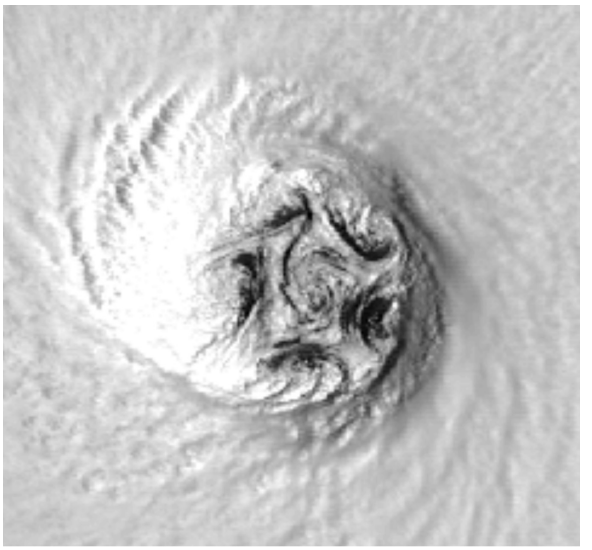

Figure 23. Defense Meteorological Satellite Program image of Hurricane Isabel at 1315 UTC 12 Sep 2003 showing the development of mesovortices radially inward of the eyewall. A similar image is shown in *Kossin and Schubert* [2004].

4. Discussion

The results of this study show that the initial development of asymmetries, and the change in $\bar{v}_{max}$ associated with that development, were not strongly influenced by the presence of moist convection. In other words, the first few hours of simulation in each moist case agreed well with the corresponding evolution in its dry counterpart. That is not to say that the diabatically driven secondary circulation has no influence on the growth of inner core asymmetries. The secondary circulation plays a vital role in organizing the vertical and radial distributions of ζ and PV, and thereby regulates the characteristics of the most unstable modes. On a longer time scale, the secondary circulation can modulate the horizontal mixing of PV.

One question that remains is why the moist secondary circulation failed to strongly affect the initial growth rates of the most unstable modes (cf. Figure 4). One possible explanation is related to the time scale of the initial growth. It was shown that the *e*-folding times during the initial exponential growth were approximately 15–20 min. This is substantially less than the convective time scale in the eyewall. Assuming an average updraft velocity of 2 m s^{-1}, it would take a parcel about 50 min to ascend to a height of 6 km. It is possible that the secondary circulation would have a larger impact for slower developing instabilities. Another possible explanation concerns the location of the cloudy updraft relative to the vorticity (PV) peak supporting the instability. Figure 22 shows *r,z* plots of the asymmetry field χ (see section 3.2.1 for an explanation of this variable) overlaid with select contours of azimuthally averaged relative humidity (*RH*) and vertical velocity (*w*) during the initial exponential growth period in the three moist simulations. The bulk of the asymmetric growth occurs in a region of unsaturated air radially inward of the eyewall updraft. Thus, it is reasonable that the moist secondary circulation should have limited direct influence on the initial exponential growth. Similar offsets between the ζ annulus and the secondary circulation are apparent in the axisymmetric simulations of *Hausman et al.* [2006] and in real-world TCs [e.g., *Rogers et al.*, 2012, 2013]. In fact, the famous starfish pattern in the inner core of Hurricane Isabel (2003) [e.g., *Kossin and Schubert*, 2004] occurs well inward of the eyewall cloud (Figure 23).

5. Summary and Conclusions

Three-dimensional simulations were performed in an idealized cloud model to advance the current understanding of how moist convection may affect the development of inner core instabilities associated with a pronounced peak in the radial distribution of vertical vorticity. To help achieve this goal, the instabilities of simulated TCs were compared to those found in dry nonconvective vortices with approximately the same primary circulations. The following results were found:

1. Moist convection appeared to have little impact on the initial exponential growth of inner core asymmetries. During the first 90 min of simulation, the growth rate of the asymmetry was similar between a moist vortex with a particular value of c_e/c_d and its dry counterpart.
2. An analysis of eddy kinetic energy revealed that, in all simulations, the primary source of KE' for the initial exponentially growing asymmetry was the radial shear of mean angular velocity. Production terms associated with the mean secondary circulation, as well as the vertical shear of the primary circulation, were small by comparison.
3. Moist simulations with larger surface drag seemed to more efficiently counteract PV mixing after the initial phase of instability. Figure 10 showed that the simulation with the smallest value of c_d produced the

© 2014. The Authors.

strongest disruption in the mean vorticity annulus and the largest (normalized) vertical vorticity in the center of the vortex. Simulations with larger drag experienced progressively smaller values of vertical vorticity near the vortex center and quicker regeneration of the vorticity annulus.

4. The fractional intensity change associated with the initial instability decreased with increasing c_d. By the end of the 36 h moist simulations, the maximum azimuthally averaged tangential velocity decreased by less than 4%. In contrast, the dry vortices all experienced a 9–17% decrease by the end of the simulations.

5. Inner core instabilities had minimal impact on the air-sea disequilibrium beneath the eyewall, as measured by the local EPI. By the end of the moist 3-D simulations, there was only a slight increase in the air-sea disequilibrium at the RMW. This is in contrast with the conclusions of *Yang et al*. [2007], who suggest that barotropic instability weakens simulated TCs by causing a structural change that diminishes downdrafts and decreases the moist entropy deficit at the air-sea interface.

6. The evolution of convection varied with the specification of c_e/c_d. Following the initial mixing event, two of the simulations (c_e/c_d=0.3 and c_e/c_d=1) experienced a substantial increase in integrated surface rain mass coinciding with the development of inner rain bands. A third simulation (c_e/c_d=0.5) produced relatively weak inner rain bands and a smaller increase in the surface rain mass.

In conclusion, moist convection did not profoundly affect the initial wave growth associated with barotropic instability in the present simulation set. At later times, the secondary circulation restores the vorticity annulus and reduces the intensity change associated with horizontal PV mixing. It is possible that moist convection may play a more prominent role in weaker vortices with slower-growing instabilities. However, the direct influence of the moist secondary circulation on the growth rates seems limited by the fact that the instabilities grow on the inner edge of the eyewall where there is minimal cloud water content and only modest vertical and radial motions.

Acknowledgments
This work was supported by NSF grants AGS-1101713 and AGS-1250533. Computational resources were provided by the San Diego Supercomputer Center through XSEDE allocation TG-AM130028 and by the National Center for Atmospheric Research through allocation UNWR0001. Simulation data is available upon request.

References

Andreas, E. L. (2011), Fallacies of the enthalpy transfer coefficient over the ocean in high winds, *J. Atmos. Sci.*, *68*(7), 1435–1445, doi:10.1175/2011JAS3714.1.

Bell, M. M., and M. T. Montgomery (2008), Observed structure, evolution, and potential intensity of category 5 Hurricane Isabel (2003) from 12 to 14 September, *Mon. Weather Rev.*, *136*(6), 2023–2046, doi:10.1175/2007MWR1858.1.

Bell, M. M., M. T. Montgomery and K. A. Emanuel (2012), AirSea enthalpy and momentum exchange at major hurricane wind speeds observed during CBLAST, *J. Atmos. Sci.*, *69*(11), 3197–3222, doi:10.1175/JAS-D-11-0276.1.

Braun, S. A., M. T. Montgomery, and Z. Pu (2006), High-resolution simulation of Hurricane Bonnie (1998). Part I: The organization of eyewall vertical motion, *J. Atmos. Sci.*, *63*(1), 19–42, doi:10.1175/JAS3598.1.

Bryan, G. H. (2008), On the computation of pseudoadiabatic entropy and equivalent potential temperature, *Mon. Weather Rev.*, *136*(12), 5239–5245, doi:10.1175/2008MWR2593.1.

Bryan, G. H. (2012), Effects of surface exchange coefficients and turbulence length scales on the intensity and structure of numerically simulated hurricanes, *Mon. Weather Rev.*, *140*(4), 1125–1143, doi:10.1175/MWR-D-11-00231.1.

Bryan, G. H., and J. M. Fritsch (2002), A benchmark simulation for moist nonhydrostatic numerical models, *Mon. Weather Rev.*, *130*(1992), 2917–2928.

Bryan, G. H., and R. Rotunno (2009), The influence of near-surface, high-entropy air in hurricane eyes on maximum hurricane intensity, *J. Atmos. Sci.*, *66*(1), 148–158, doi:10.1175/2008JAS2707.1.

Chen, Y., and M. K. Yau (2001), Spiral bands in a simulated hurricane. Part I: Vortex Rossby wave verification, *J. Atmos. Sci.*, *58*(15), 2128–2145, doi:10.1175/1520-0469(2001)058¡2128:SBIASH¿2.0.CO;2.

Emanuel, K. A. (1995), Sensitivity of tropical cyclones to surface exchange coefficients and a revised steady-state model incorporating eye dynamics, *J. Atmos. Sci.*, *52*(22), 3969–3976, doi:10.1175/1520-0469(1995)052¡3969:SOTCTS¿2.0.CO;2.

Hausman, S. A., K. V. Ooyama, and W. H. Schubert (2006), Potential vorticity structure of simulated hurricanes, *J. Atmos. Sci.*, *63*(1), 87–108, doi:10.1175/JAS3601.1.

Hendricks, E. A., and W. H. Schubert (2010), Adiabatic rearrangement of hollow PV towers, *J. Adv. Model. Earth Syst.*, *2*, 8, doi:10.3894/JAMES.2010.2.8.

Hendricks, E. A., W. H. Schubert, R. K. Taft, H. Wang, and J. P. Kossin (2009), Life cycles of hurricane-like vorticity rings, *J. Atmos. Sci.*, *66*(3), 705–722, doi:10.1175/2008JAS2820.1.

Hendricks, E. A., B. D. McNoldy, and W. H. Schubert (2012), Observed inner-core structural variability in hurricane dolly (2008)*, *Mon. Weather Rev.*, *140*(12), 4066–4077, doi:10.1175/MWR-D-12-00018.1.

Hendricks, E. A., W. H. Schubert, Y.-H. Chen, H.-C. Kuo, and M. S. Peng (2014), Hurricane eyewall evolution in a forced shallow water model, *J. Atmos. Sci.*, *71*, 1623–1643, doi:10.1175/JAS-D-13-0303.1.

Kossin, J., and M. Eastin (2001), Two distinct regimes in the kinematic and thermodynamic structure of the hurricane eye and eyewall, *J. Atmos. Sci.*, *58*, 1079–1090.

Kossin, J. P., and W. H. Schubert (2004), Mesovortices in Hurricane Isabel, *Bull. Am. Meteorol. Soc.*, *85*(2), 151–153, doi:10.1175/BAMS-85-2-151.

Kwon, Y. C., and W. M. Frank (2005), Dynamic instabilities of simulated hurricane-like vortices and their impacts on the core structure of hurricanes. Part I: Dry experiments, *J. Atmos. Sci.*, *62*(11), 3955–3973, doi:10.1175/JAS3575.1.

© 2014. The Authors.

Kwon, Y. C., and W. M. Frank (2008), Dynamic instabilities of simulated hurricane-like vortices and their impacts on the core structure of hurricanes. Part II: Moist Experiments, *J. Atmos. Sci.*, *65*(1), 106–122, doi:10.1175/2007JAS2132.1.

Michalke, A., and A. Timme (1967), On the inviscid instability of certain two-dimensional vortex-type flows, *J. Fluid Mech.*, *29*(04), 647, doi:10.1017/S0022112067001090.

Montgomery, M. T., and L. J. Shapiro (1995), Generalized Charney-Stern and Fjortoft theorems for rapidly rotating vortices, *J. Atmos. Sci.*, *52*(10), 1829–1833, doi:10.1175/1520-0469(1995)052¡1829:GCAFTF¿2.0.CO;2.

Montgomery, M. T., M. M. Bell, S. D. Aberson, and M. L. Black (2006), Hurricane Isabel (2003): New insights into the physics of intense storms. Part I: Mean vortex structure and maximum intensity estimates, *Bull. Am. Meteorol. Soc.*, *87*(10), 1335–1347, doi:10.1175/BAMS-87-10-1335.

Muramatsu, T. (1986), The structure of polygonal eye of a typhoon, *J. Meteorol. Soc. Jpn.*, *64*, 913–921.

Nolan, D., and B. Farrell (1999), Generalized stability analyses of asymmetric disturbances in one- and two-celled vortices maintained by radial inflow, *J. Atmos. Sci.*, *56* 1282–1307.

Nolan, D. S. (2012), Three-dimensional instabilities in tornado-like vortices with secondary circulations, *J. Fluid Mech.*, *711*, 61–100, doi:10.1017/jfm.2012.369.

Nolan, D. S., and M. T. Montgomery (2002), Nonhydrostatic, three-dimensional perturbations to balanced, hurricane-like vortices. Part I: Linearized formulation, stability, and evolution, *J. Atmos. Sci.*, *59*(21), 2989–3020, doi:10.1175/1520-0469(2002)059¡2989:NTDPTB¿2.0.CO;2.

Persing, J., M. T. Montgomery, J. C. McWilliams, and R. K. Smith (2013), Asymmetric and axisymmetric dynamics of tropical cyclones, *Atmos. Chem. Phys.*, *13*(24), 12,299–12,341, doi:10.5194/acp-13-12299-2013.

Reasor, P. D., M. T. Montgomery, F. D. Marks, and J. F. Gamache (2000), Low-wavenumber structure and evolution of the hurricane inner core observed by airborne dual-Doppler radar, *Mon. Weather Rev.*, *128*(6), 1653–1680.

Rogers, R., S. Lorsolo, P. Reasor, J. Gamache, and F. Marks (2012), Multiscale analysis of tropical cyclone kinematic structure from airborne Doppler radar composites, *Mon. Weather Rev.*, *140*(1), 77–99, doi:10.1175/MWR-D-10-05075.1.

Rogers, R., P. Reasor, and S. Lorsolo (2013), Airborne Doppler observations of the inner-core structural differences between intensifying and steady-state tropical cyclones, *Mon. Weather Rev.*, *141*(9), 2970–2991, doi:10.1175/MWR-D-12-00357.1.

Rotunno, R. (1978), A note on the stability of a cylindrical vortex sheet, *J. Fluid Mech.*, *87*(4), 761–771.

Rotunno, R., and K. A. Emanuel (1987), An AirSea interaction theory for tropical cyclones. Part II: Evolutionary study using a nonhydrostatic axisymmetric numerical model, *J. Atmos. Sci.*, *44*(3), 542–561, doi:10.1175/1520-0469(1987)044¡0542:AAITFT¿2.0.CO;2.

Rozoff, C. M., J. P. Kossin, W. H. Schubert, and P. J. Mulero (2009), Internal control of hurricane intensity variability: The dual nature of potential vorticity mixing, *J. Atmos. Sci.*, *66*(1), 133–147, doi:10.1175/2008JAS2717.1.

Schecter, D. A. (2013), Relationships between convective asymmetry, imbalance and intensity in numerically simulated tropical cyclones, *Tellus Ser. A*, *1*, 1–18, doi:10.3402/tellusa.v65i0.20168.

Schecter, D. A., and M. T. Montgomery (2007), Waves in a cloudy vortex, *J. Atmos. Sci.*, *64*(2), 314–337, doi:10.1175/JAS3849.1.

Schecter, D. A., D. H. E. Dubin, K. S. Fine, and C. F. Driscoll (1999), Vortex crystals from 2D Euler flow: Experiment and simulation, *Phys. Fluids*, *11*, 905–914.

Schubert, W. H., M. T. Montgomery, R. K. Taft, T. A. Guinn, S. R. Fulton, J. P. Kossin, and J. P. Edwards (1999), Polygonal eyewalls, asymmetric eye contraction, and potential vorticity mixing in hurricanes, *J. Atmos. Sci.*, *56*(9), 1197–1223, doi:10.1175/1520-0469(1999)056¡1197:PEAECA¿2.0.CO;2.

Smith, P. L., C. G. Myers, and H. D. Orville (1975), Radar reflectivity factor calculations in numerical cloud models using bulk parameterization of precipitation, *J. Appl. Meteorol.*, *14*(6), 1156–1165, doi:10.1175/1520-0450(1975)014¡1156:RRFCIN¿2.0.CO;2.

Wang, Y. (2002), Vortex Rossby waves in a numerically simulated tropical cyclone. Part I: Overall structure, potential vorticity, and kinetic energy budgets*, *J. Atmos. Sci.*, *59*(7), 1213–1238, doi:10.1175/1520-0469(2002)059¡1213:VRWIAN¿2.0.CO;2.

Wang, Y. (2007), A multiply nested, movable mesh, fully compressible, nonhydrostatic tropical cyclone model TCM4: Model description and development of asymmetries without explicit asymmetric forcing, *Meteorol. Atmos. Phys.*, *97*(1-4), 93–116, doi:10.1007/s00703-006-0246-z.

Williams, G. J., R. K. Taft, B. D. McNoldy, and W. H. Schubert (2013), Shock-like structures in the tropical cyclone boundary layer, *J. Adv. Model Earth Syst.*, *5*, 338–353, doi:10.1002/jame.20028.

Yang, B., Y. Wang, and B. Wang (2007), The effect of internally generated inner-core asymmetries on tropical cyclone potential intensity*, *J. Atmos. Sci.*, *64*(4), 1165–1188, doi:10.1175/JAS3971.1.

Zhu, P., K. Menelaou, and Z. Zhu (2013), Impact of subgrid-scale vertical turbulent mixing on eyewall asymmetric structures and mesovortices of hurricanes, *Q. J. R. Meteorol. Soc.*, *140*(679), 416–438, doi:10.1002/qj.2147.

© 2014. The Authors.